Geophysical Journal International

Royal Astronomical Society

Geophys. J. Int. (2025) 241, 1494–1517 Advance Access publication 2025 March 28 GJI Seismology

https://doi.org/10.1093/gji/ggaf119

A stress model for nonlinear reservoir compaction and application to the post shut-in Groningen gas field

F.M. Aben⁶, J.P. Pruiksma, D. Kraaijpoel, S. Osinga¹ and M.P.D. Pluymaekers¹

 ${}^1\mathit{TNO-GDN}\ Geological\ Survey\ of\ the\ Netherlands,\ 3584CB\ Utrecht,\ The\ Netherlands.\ E-mail:\ frans.aben@tno.nl}$

Accepted 2025 March 16. Received 2025 March 15; in original form 2024 October 3

SUMMARY

Seismic source models that use an elastic relation between pressure decrease, compaction and stress change have been shown to successfully reproduce induced seismicity in producing natural gas reservoirs undergoing differential compaction. However, this elastic relation is inconsistent with observations of nonlinear reservoir compaction in the Groningen field. We utilize critical state mechanics theory to derive a 3-D stress-strain framework that is able to house 1-D nonlinear stress-strain relations typically used for subsidence models, without the need for recalibration of the subsidence model parameters. This is used to adapt the elastic thin sheet stress model that is currently in use as the state-of-the-art for seismicity predictions as part of the hazard and risk assessment of the Groningen gas field. The new thin sheet model has one additional model parameter that modulates the impact of inelastic deformation on fault loading, whilst keeping the intended function of the model calibration from the original elastic thin sheet model intact. The resulting elastic-viscoplastic thin sheet stress model is consistent with previously reported nonlinear rate-dependent reservoir compaction in Groningen found from inverting subsidence data and from rock deformation experiments. Our elastic-viscoplastic thin sheet stress model is able to predict ongoing stress increase, and therefore ongoing seismicity, in areas where pressure does not decrease anymore due to shutin. A pseudo-prospective forecasting exercise indeed shows that the elastic-viscoplastic stress model performs better than the linear elastic stress model. This model addition ensures that the Groningen seismic source model is well suited for predicting seismicity in the post shut-in phase.

Key words: Creep and deformation; Geomechanics; Earthquake interaction, forecasting, and prediction; Induced seismicity.

1 INTRODUCTION

Differential compaction between fault-bounded reservoir compartments is a mechanism for induced seismicity in reservoirs during pore pressure depletion (Pennington *et al.* 1986; Suckale 2009). Seismicity caused by differential compaction occurred, amongst others, in hydrocarbon reservoirs in South-Central Texas (Davis *et al.* 1995), gas fields in Northern Germany (Haug *et al.* 2018), and gas fields in the Netherlands (e.g. Roest & Mulders 2000; Mulders 2003; Van Wees *et al.* 2014). The latter includes the arguably most studied example of compaction-induced seismicity, the Groningen gas field (e.g. van Thienen-Visser & Breunese 2015). Hence, a number of seismic source models for compaction-induced seismicity were specifically developed for the Groningen field (for a recent overview, see Kühn *et al.* 2022). Of these numerous models, physics-informed models (or 'hybrid' models in Kühn *et al.* 2022's nomenclature) combine physical concepts with

statistical fitting of the observed data, that is, the catalogue of observed earthquakes. These are well equiped for use in probabilistic forecasting of spatio-temporal(-magnitudal) earthquake event rates. These physics-informed models typically consist of a stress model in which stressing of faults is calculated, and an activity rate model that relates these stress changes to seismicity rates (e.g. Bourne & Oates 2017; Dempsey & Suckale 2017; Candela *et al.* 2019; Heimisson *et al.* 2022). The physics-informed model by Bourne & Oates (2017) and Bourne *et al.* (2018) is used in the annual probabilistic seismic hazard and risk analyses (pSHRA) for the Groningen region (TNO 2023, for the latest edition) and is considered state-of-the-art.

Here, we focus on an improvement of the stress model, which uses as input reservoir pressure changes and vertical reservoir compaction. Reservoir compaction is inferred from surface subsidence observations using workflows that are comprised of the relation between pressure change and reservoir compaction at depth, and a transfer function for the reservoir compaction's surface expression

²TNO Mobility and Built Environment, 2629JD Delft, The Netherlands

(e.g. van Thienen-Visser et al. 2015; van Eijs & van der Wal 2017; Fokker et al. 2018). In these workflows, an essentially 1-D relation between vertical stress (i.e. pressure change) and vertical strain (i.e. compaction) is sufficient to obtain the desired subsidence. Examples of these 1-D relations are, amongst others, the bi-linear model (Hettema et al. 2002), time-decay model (Mossop 2012), the Rate Type isotach compaction model (Pruiksma et al. 2015), or (variations on) Burgers models (e.g. Jiang & Wang 2022; Cavalié et al. 2023), as well as a straightforward linear poro-elastic relation. Aside from the linear model, the other models have a non-linear, often ratedependent, relation between pressure and compaction, in addition to a linear elastic component. For Groningen, the phenomenology of these nonlinear rate-dependent models, specifically the time-decay and Rate Type isotach compaction models, are in agreement with experimental observations of rate-dependent inelastic deformation on Groningen's Slochteren sandstone or its analogues (de Waal 1986; Hol et al. 2015; Shinohara et al. 2024). Indeed, several studies find that the 1-D non-linear rate-dependent relations between pressure and compaction fit best with the observed subsidence data for Groningen (e.g. van Thienen-Visser & Fokker 2017; van Eijs & van der Wal 2017). Note that 'instanteneous' inelastic deformation in Slochteren sandstone was experimentally identified as well (Pijnenburg et al. 2019), but it cannot (yet) be distinguished from elastic deformation when using subsidence observations.

Contrary to subsidence- and laboratory observations, the current inventory of Groningen seismic source models lack nonlinear stress-strain relations. This leads to inconsistencies between subsidence models and seismic source models, and their respective forecasts. Moreover, a seismic source model based on a linear elastic stress-strain relation may miss stress increase by inelastic ratedependent deformation as an additional driver for seismicity. This is particularly important for areas where pore pressure reduction as the primary driver is absent—a distinct possibility with the recent shut-in of the Groningen field (per 2023 October 1). The remaining drivers for pressure change, internal pressure reequilibration and recharge from bounding aquifers, are likely to result in areas of constant pressure or pressure increase instead of pressure decrease. The main aim of this work is to solve this inconsistency by incorporating pre-existing, already calibrated, nonlinear 1D relations into the stress calculation of a seismic source model for Groningen.

The challenge lies in the fact that a 1-D stress-strain relation is not sufficient for a stress model, where a full 3-D stress-strain relation is required to compute fault loading. The current seismic source models for Groningen with linear poro-elastic reservoir compaction handle this problem by an easy transformation to a 3-D relation using Hooke's law in combination with certain boundary conditions. These models thus either adopt a 1-D linear subsidence model in their workflow (e.g. Smith et al. 2019, 2022), or utilize subsidence inversion results from previous work (e.g. Bourne & Oates 2017 use results by Bierman et al. 2015). For the nonlinear models, comprised of a linear elastic and a nonlinear inelastic strain term, the 'upscaling' to a 3-D stress-strain relation is less trivial, as it requires information on how the 1-D inelastic strain is coupled to the other inelastic strain tensor components. A 1-D model, by definition, lacks this information. We therefore assume that the reservoir rock adheres to the concept of critical state mechanics (e.g. Wood 1990; Atkinson 1993), from which we derive a framework to fit in these 1-D nonlinear models, partly following the approach outlined by Vermeer & Neher (1999) and Isotton et al. (2019). This allows us to define a parameter to describe the relation between the vertical inelastic strain and the other inelastic strain tensor components. The framework is incorporated into the formulation of the thin sheet stress model of Bourne & Oates (2017), where we aim to retain the physical meaning and function of pre-existing model calibration parameters, whilst keeping the number of new model calibration parameters to a minimum for efficient model calibration. Note that here we equate the term viscoplasticity (used in critical state mechanics literature) with rate-dependent inelastic deformation.

The development of the 3-D stress-strain framework and its implementation in the thin sheet stress model forms the main body of this work. Although our work was carried out in the context of induced seismicity in the Groningen gas field, with the specifics and simplifications of Bourne & Oates (2017)'s thin sheet stress model in mind, we note that this stress-strain framework can receive any 1-D subsidence model that yields total strain as the sum of elastic and inelastic strains. Next, we show how the resulting stress curves from the expanded thin sheet stress model are impacted by model parameter variations, by adopting as input for compaction behaviour the most recently calibrated version of the Rate Type isotach model (NAM 2021). Finally, the expanded thin sheet stress model is used as part of the probabilistic seismic source model by Bourne & Oates (2017) and Bourne et al. (2018) to produce seismicity event rates. These rates are used in a model comparison exercise with the currently used elastic seismic source model.

2 APPROACH TO DEVELOPMENT OF MODELS

In this section, we discuss briefly the thin sheet geometry and its assumptions (Section 2.1). We then present the data used for the parameter exploration of the models and the various figures in the manuscript (Section 2.2). This section concludes by presenting the definitions of stress and strain used in the derivation of the new model (Section 2.3). In Section 3, we recap the original poro-elastic thin sheet model of Bourne & Oates (2017), and showcase the impact of the model parameters on temporal and spatial stress distributions. The expansion to an elastic-viscoplastic thin sheet model is presented in Section 4, including a similar parameter exploration on temporal and spatial stress distributions.

2.1 Thin sheet geometry and assumptions

We rederive the poro-elastic thin sheet stress model of Bourne & Oates (2017) to allow for inelastic deformation in addition to elastic deformation. The thin sheet approximation for a reservoir allowed Bourne & Oates (2017), and allows us now, to simplify the equations for Coulomb stress changes. The reservoir is a laterally infinite and geometrically homogeneous layer with isotropic material properties-that is, the thin sheet-embedded in a linear elastic halfspace. These assumptions are justified given that the lateral extent of the Groningen reservoir (of the order of 10s of kms) is much larger than its thickness (of the order of 100s of ms). The largest compressive principal stress is oriented vertically, in line with the extensional tectonic stress regime of the region. From the thin sheet symmetry follows a uniaxial strain condition without horizontal strain. A rotational symmetry is invoked as well, so that the two horizontal principal stresses are equal to each other. Stresses and strains in the thin sheet can be considered as the vertically averaged stresses and strains over the thickness of the reservoir, effectively eliminating the depth dimension.

However, in the derivations by Bourne & Oates (2017) and what will be presented here, the conditions that follow from the thin sheet

geometry are, strictly speaking, violated by allowing for lateral variations in elastic compressibility, pressure, reservoir thickness and reservoir depth. This results in loss of symmetry leading to rotation of principal stresses and strains, and a non-vanishing horizontal strain that infringes on the convenient uniaxial strain condition. We consider these variations to be smooth relative to the thickness of the thin sheet, so that the resulting deviations in stress relative to the uniaxial situation are small. Hence, the conceptual picture of how stress evolves over time does not change.

Faults do not fall into the category of smooth lateral deviations but are strong, local deviations from the uniaxial case. In Bourne & Oates (2017), these deviations are accounted for in two ways: (1) Stress resulting from the thin sheet model is explicitly amplified at the location of faults based on specific fault properties such as fault offset and local reservoir thickness (see section 2.3 in Bourne & Oates 2017). (2) Deviations relative to the uniaxial situation are absorbed in the stochastic variations of Coulomb stress, properly represented in the extreme threshold failure activity rate model (Bourne & Oates 2017) (or any other probabilistic activity rate model). The stochastic variations also represent initial Coulomb stress and fault strength (Bourne & Oates 2017). In this manuscript, we keep this same approach for handling faults in the thin sheet model, so that only the thin sheet model with smooth lateral variations needs to be adopted for inelastic deformation.

2.2 Data used for model parameter exploration

The developed elastic-viscoplastic model will contain several parameters on which resides an uncertainty, the so-called model calibration parameters. To study the impact of these parameters on the behaviour of the resulting stresses in space and time, a small parameter exploration is conducted once the model has been developed.

To do so, we utilize model input from the Groningen reservoir. The input is comprised of the compaction coefficient grid and the pressure history. The compaction coefficients are obtained by inversion of surface subsidence data and pressure data, where subsidence data has been measured for decades by regular levelling measurement campaigns. Such compaction coefficient grids are updated regularly, we utilize the results of the study by NAM (2021), which follows the method of van Eijs & van der Wal (2017). Note that these studies fit 1D non-linear models to the subsidence data, consisting of an elastic part and inelastic part. The elastic part yields the static compaction coefficient grid (c_m^e) , which includes lateral variations in compressibility (Fig. 1a).

The pressure histories are history-matched reservoir simulation results provided by the operator of the field (NAM), the data can be found at Zenodo (2023) and details on the history matching at Landman & Vissers (2023). Historically, production was planned in so-called 'gas years', year-long periods that run from 1st of October until the 30th of September the following year. The pressure record is discretized in these gas years, and spans a time period starting in gas year 1957 (i.e. 1957 October 1) until gas year 2053 (ending on 2054 September 30). The reservoir pressure history is roughly as follows (inset in Fig. 1b): Pressure remains relatively stable up to the mid-1960s when production is ramped up. This is the onset of decades of pressure reduction, up to the end of the 2010s, where production was reduced significantly towards a planned shut-in. In this period, between 2018 and 2023, pressure in parts of the field stabilize and even increases at some localities. Stabilization and pressure increase are driven by internal pressure equilibration of the reservoir as well as in-flow from bounding aquifers connected to the reservoir. Shut-in occurred at the start of gas year 2023: From then until the end of the pressure simulation results, the pressure equilibrates everywhere in the reservoir, characterised by areas of decelerating pressure increase, decelerating pressure decrease, and stable pressure.

We shall compare stress change solutions by normalizing them, as the shape of the curve are most informative: Given an activity rate model with instant stress threshold failure (such as the preferred extreme threshold failure model currently used in the Groningen SHRA), only an increasing stress results in modelled seismicity. We also note that for many activity rate models, the relative stress change is more important rather than the absolute stress magnitudes, as some form of normalization by a model parameter occurs. For the figures here, normalization is done so that the stress at the onset of production is 0 and the stress at the end of the pressure history (gas year 2053) is 1.

2.3 Definitions of strain and stress

We adopt the convention that compressive stress and contractional strain are negative and depletion is a negative change in pore pressure. The chosen stress metric for seismicity in Bourne & Oates (2017) is the maximum Coulomb stress on an optimally oriented fault:

$$C = C_0 + \Delta C,\tag{1}$$

where C_0 is the initial Coulomb stress prior to the onset of gas production and ΔC the change in Coulomb stress caused by subsurface activity (gas extraction, injection or post-production pressure equilibration) relative to the pre-production state. Note that other stress metrics may be adopted depending on the activity rate model. Here, we use the extreme threshold failure activity model (Bourne & Oates 2017), which acknowledges that C_0 has an unknown distribution over the reservoir's fault segments, where it is assumed that failure occurs only on fault segments with a value of C_0 in the tail of this distribution (fig. 2 in Bourne & Oates 2017). Hence, the quantity of interest is ΔC , and we will look at incremental stress and pressure changes rather than absolute values:

$$\Delta C = \underbrace{\Delta \tau}_{\text{applied stress}} + \underbrace{\mu(\Delta \sigma_{\text{n}} + \alpha \Delta p_{\text{f}})}_{\text{fault strength}}, \tag{2}$$

where the applied stress on the fault is given by the maximum shear stress $\Delta \tau$ and the resistance to sliding is given by the friction coefficient μ and the mean normal stress $\Delta \sigma_n$ corrected for the pore pressure Δp_f times Biot's coefficient α .

Incremental effective stress changes are given as

$$\Delta \sigma^{\text{eff}} = \Delta \sigma + \alpha \Delta p_{\text{f}}. \tag{3}$$

It follows from a constant overburden that $\Delta\sigma_{\rm v}=0$, so that vertical effective stress change is fully determined by pore pressure variations as $\Delta\sigma_{\rm v}^{\rm eff}=\alpha\Delta p_{\rm f}$. Given these changes in principal stresses, eq. (2) changes to:

$$\Delta \tau = \frac{1}{2} (\Delta \sigma_{h} - \Delta \sigma_{v}) = \frac{1}{2} \Delta \sigma_{h},$$

$$\Delta \sigma_{n} = \frac{1}{2} (\Delta \sigma_{h} + \Delta \sigma_{v}) = \frac{1}{2} \Delta \sigma_{h},$$

$$\Delta C = \frac{1 + \mu}{2} \Delta \sigma_{h} + \mu \alpha \Delta p_{f}.$$
(4)

As can be seen, the Coulomb stress change depends on changes in horizontal stress and pore pressure. In the derivation by Bourne

elastic thin sheet model spatial distribution of horizontal stress change

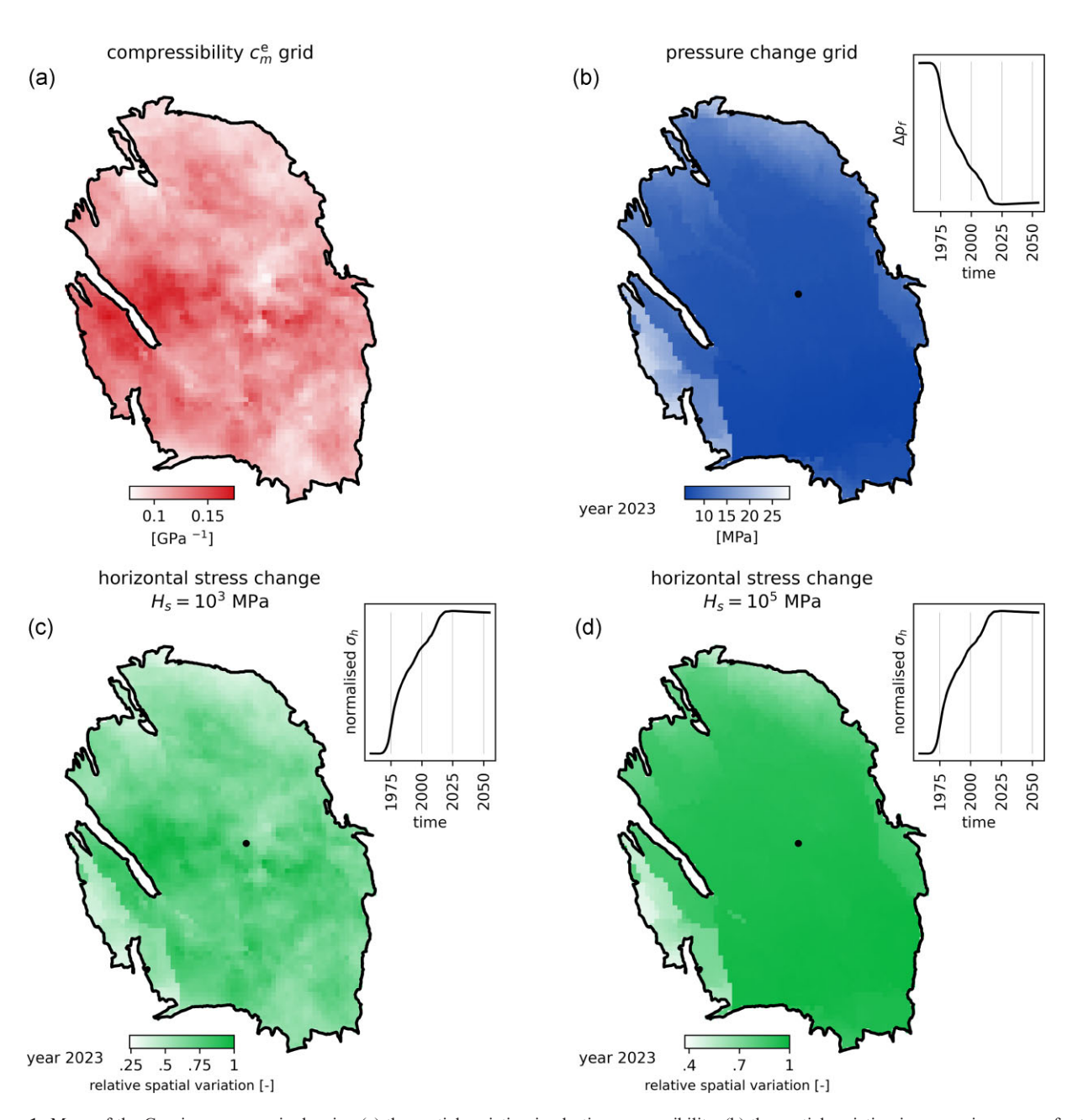


Figure 1. Maps of the Groningen reservoir showing (a) the spatial variation in elastic compressibility, (b) the spatial variation in reservoir pressure for the gas year 2023 and (c, d) the distribution of relative horizontal stress change for a low (c) and high (d) value of model parameter H_s for gas year 2023. Stress changes are normalized to the largest stress change for this gas year. The insets at (b–d) show the pressure and stress change history at a point in the centre of the field (black marker).

& Oates (2017), the pore pressure term becomes negligble at their eqs (22) and (57), when geometrical heterogeneities (i.e. faults) are implemented, and can thus be discarded. By doing so, the Coulomb stress is proportional to the change in horizontal stress. Inelastic behaviour would not affect this pore pressure term (assuming rate-dependent inelastic deformation is sufficiently slow for drained conditions), but only affects the horizontal stress term. In the derivation that follows, we shall focus on the change in σ_h or σ_h^{eff} , in the knowledge that this directly corresponds to ΔC when discarding $\mu \alpha \Delta p_f$.

If one chooses not to discard said term, the final result from our derivation would simply need to be augmented by it.

Critical state mechanics typically uses two invariants of the stress tensor, the effective mean stress *P* and differential stress *Q*:

$$\Delta P = (\Delta \sigma_{\rm v}^{\rm eff} + 2\Delta \sigma_{\rm h}^{\rm eff})/3 = (\alpha \Delta p_{\rm f} + 2\Delta \sigma_{\rm h}^{\rm eff})/3,$$

$$\Delta Q = \Delta \sigma_{\rm v}^{\rm eff} - \Delta \sigma_{\rm h}^{\rm eff} = \alpha \Delta p_{\rm f} - \Delta \sigma_{\rm h}^{\rm eff}.$$
(5)

Total strain $\varepsilon^{\text{total}}$ is the sum of the individual strain components (e.g. elastic strain ε^{e} and/or inelastic strain ε^{i}). The thin sheet geometry has a uniaxial strain boundary condition, so that total horizontal strain $\varepsilon^{\text{total}}_{\text{h}} = 0$.

3 ELASTIC THIN SHEET MODEL

What follows in this section is a recap of the elastic thin sheet stress model by Bourne & Oates (2017), presented here to provide a foundation to the development of the elastic-viscoplastic thin sheet stress model in the next section.

Total strain $\varepsilon^{\text{total}}$ consists solely of the elastic strain component $\varepsilon^{\text{e}}_{\text{h}}$. From poroelasticity in an isotropic medium, the incremental elastic horizontal and vertical strains are a function of two elastic parameters:

$$\Delta \varepsilon_{\rm v}^{\rm e} = \frac{1}{E} (\Delta \sigma_{\rm v}^{\rm eff} - 2\nu \Delta \sigma_{\rm h}^{\rm eff}) = \frac{1}{E} (\alpha \Delta p_{\rm f} - 2\nu \Delta \sigma_{\rm h}^{\rm eff}),$$

$$\Delta \varepsilon_{\rm h}^{\rm e} = \frac{1}{E} (\Delta \sigma_{\rm h}^{\rm eff} - \nu (\Delta \sigma_{\rm h}^{\rm eff} + \Delta \sigma_{\rm v}^{\rm eff})) = \Delta \sigma_{\rm h}^{\rm eff} \frac{1 - \nu}{E} - \alpha \Delta p_{\rm f} \frac{\nu}{E},$$
(6)

where E is Young's modulus and ν is Poisson's ratio. Applying the uniaxial strain boundary conditions ($\varepsilon_h^{\text{total}} = \varepsilon_h^{\text{e}} = 0$) gives the expression for the horizontal stress and horizontal effective stress:

$$\Delta \sigma_{\rm h} = -\alpha \Delta p_{\rm f} \frac{1 - 2\nu}{1 - \nu},$$

$$\Delta \sigma_{\rm h}^{\rm eff} = \alpha \Delta p_{\rm f} \frac{\nu}{1 - \nu}.$$
(7)

Substituting this expression in eq. (4) gives the Coulomb stress change in a homogeneous elastic thin sheet. Combining eq. (7) and eq. (6) gives the vertical elastic strain:

$$\Delta \varepsilon_{\rm v}^{\rm e} = \frac{1}{E} \frac{(1+\nu)(1-2\nu)}{(1-\nu)} \alpha \Delta p_{\rm f} = \frac{1}{H} \alpha \Delta p_{\rm f}, \tag{8}$$

where the elastic term H is known as the uniaxial compaction modulus (Figer *et al.* 2008).

Whereas the pore pressure change in eq. (7) is considered a known quantity, Biot's coefficient α and its spatial variation throughout the reservoir is not. Following Bourne & Oates (2017), we shall eliminate α and introduce H by simply rewriting eq. (8) as:

$$\alpha \Delta p_{\rm f} = H \Delta \varepsilon_{\rm u}^{\rm e}.\tag{9}$$

and substituting $\alpha \Delta p_f$ in eq. (7) to obtain the stress change:

$$\Delta \sigma_{\rm h}^{\rm eff} = H \Delta \varepsilon_{\rm v}^{\rm e} \frac{\nu}{1 - \nu}.$$
 (10)

Note that P and Q in eq. (5) follow the same substitution:

$$\Delta P = \left(H\Delta\varepsilon_{\rm v}^{\rm e} + 2\Delta\sigma_{\rm h}^{\rm eff}\right)/3,$$

$$\Delta Q = H\Delta\varepsilon_{\rm v}^{\rm e} - \Delta\sigma_{\rm h}^{\rm eff}.$$
(11)

Parameter *H* can be further defined by first looking at the definition of the Biot's coefficient:

$$\alpha = 1 - K/K_{\rm s},\tag{12}$$

where K_s is the bulk modulus of the solid skeleton and $K < K_s$. For $K_s \gg K$, $\alpha = 1$, and the coupling between pore pressure change and horizontal stress change (eq. 7) is efficient. For a higher value of K relative to K_s , the coupling is less efficient, 'damping' pore pressure effects on the stress change. For some given lateral variations of K in our thin sheet, a comparatively low value of K_s gives relatively large lateral variations in α , so that the lateral heterogeneities are expressed in the spatial distribution of the horizontal stress (and, by extension following eq. 4, in the Coulomb stress). For a comparatively high value of K_s , the lateral variations in α are small,

and thus the heterogeneities disappear in the spatial distribution of the horizontal stresses. The variations in K and α are not directly known, but α can be rewritten as:

$$\frac{1}{K} = \frac{1}{K}\alpha + \frac{1}{K_s},\tag{13}$$

or, for uniaxial strain conditions in an elastic medium, as

$$\frac{1}{H} = \frac{1}{H}\alpha + \frac{1}{H_s},\tag{14}$$

where H_s is the uniaxial compaction modulus of the solid skeleton. From eq. (8) we see that the first term in eq. (14) is simply the ratio of change in elastic strain and change in pore pressure,

$$\frac{\Delta \varepsilon_{\rm v}^{\rm e}}{\Delta p_{\rm f}} = \frac{1}{H} \alpha = \frac{1}{H_{\rm r}} = c_{\rm m}^{\rm e},\tag{15}$$

also known as elastic compaction coefficient $c_{\rm m}^{\rm e}$, which is a typical result from subsidence studies where $c_{\rm m}^{\rm e}$ is produced in the form of a spatial map (see Fig. 1a for the $c_{\rm m}^{\rm e}$ -map of the Groningen reservoir obtained by NAM 2021). Using eqs (14) and (15) to define H in eq. (10), we have thus introduced known lateral variations in poroelasticity into the modelled stress field.

In Bourne & Oates (2017), H_s is utilized as a model calibration parameter to modulate the spatial distribution of the Coulomb stress. The effect of H_s on the Coulomb stress distribution for an elastic thin sheet is shown in Fig. 1: For $H_s \ll H_r$, the detailed spatial variation present in the observed compaction (Fig. 1a) is visible in the stress distribution (Fig. 1c) in addition to the spatial variations in pore pressure change. For $H_s \gg H_r$, the spatial Coulomb stress (Fig. 1b) mirrors the spatial distribution of pore pressure changes only (Fig. 1d). The temporal evolution of the normalized horizontal stress follows that of the pressure change, regardless of the value chosen for H_s (Figs 1b and c, insets).

4 ELASTIC-VISCOPLASTIC THIN SHEET MODEL

4.1 Strain in an elastic-viscoplastic thin sheet

In this section, we introduce the inelastic component into the thin sheet model. To allow for either plastic (i.e. instantenously inelastic) or viscoplastic (rate-dependent inelastic) strains, the strains and stresses defined in Section 2.3 are now expressed as rates instead of incremental changes. The total strain rate is the sum of the elastic strain rate and inelastic strain rate:

$$\dot{\varepsilon}^{\text{total}} = \dot{\varepsilon}^{\text{e}} + \dot{\varepsilon}^{\text{i}},\tag{16}$$

and the horizontal strain rate adheres to the uniaxial boundary condition $\dot{\varepsilon}_h^{\rm total}=0$. As we deviate from linear elasticity into nonlinear stress–strain behaviour, the outcome of the model may depend on the initial stress and strain conditions, for which we use the subscript $_0$. The differential equation that is developed here will return the absolute (effective) horizontal stress, rather than the incremental change. Nonetheless, the activity rate model requires the stress change, and so results in this section are shown as normalized stress changes.

We assume that the reservoir rock adheres to the concept of critical state soil mechanics (e.g. Wood 1990; Atkinson 1993), a framework that unifies changes in effective stresses and inelastic volumetric strain. The 'critical state' refers to a particular combination of effective stresses (the critical state line) where the plastic volumetric strain is zero, and only plastic shear strain exists. Although

designed for soils, critical state mechanics captures the empirical elastic—plastic behaviour of porous consolidated rock quite well (e.g. Nguyen et al. 2014; Cassiani et al. 2017). Inelastic deformation commences at a certain stress state described by a stress tensor or its invariants. This condition is reached when $f(P, Q, P^*) = 0$, where f describes the yield envelope (also known as yield function or 'cap') in P-Q space bounding the elastic-only deformation domain (Wood 1990). Yield function f can be parametrized in various ways. In Section 4.3, we will adopt a specific parametrization of the yield function f. P^* is the hydrostatic mean stress at the onset of inelastic deformation (also known as preconsolidation pressure in geotechnical engineering). The plastic potential is described by function g, so that the strain rate components follow the flow rule

$$\dot{\varepsilon}_{ij}^{\rm i} = \Lambda \frac{\partial g}{\partial \sigma_{ii}^{\rm eff}},\tag{17}$$

where Λ is a scalar flow rate multiplier. We consider the hardening rule, required to derive Λ , as an implicit part of the selected 1-D inelastic model. Another condition, that of being in a state of plastic yield where f=0, is also implicit to most 1-D elastic-viscoplastic models; inelastic deformation occurs from the onset in addition to elastic deformation. However, the yield condition is for a 1-D stress state, and not for a stress tensor. With the above, we shall derive a 3-D framework for 1-D elastic-viscoplastic models, following the approach of Vermeer & Neher (1999) (see also Isotton *et al.* 2019; Musso *et al.* 2021).

First, we define the plastic potential as $g = P^*$ (Vermeer & Neher 1999; Isotton *et al.* 2019), so that eq. (17) can be expressed as:

$$\Lambda \frac{\partial g}{\partial \sigma_{ij}^{\text{eff}}} = \Lambda \frac{\partial P^*}{\partial \sigma_{ij}^{\text{eff}}} = \Lambda \left(\frac{\partial P^*}{\partial P} \frac{\partial P}{\partial \sigma_{ij}^{\text{eff}}} + \frac{\partial P^*}{\partial Q} \frac{\partial Q}{\partial \sigma_{ij}^{\text{eff}}} \right), \tag{18}$$

where

$$\frac{\partial P}{\partial \sigma_{ij}^{\text{eff}}} = -\frac{1}{3} \delta_{ij},
\frac{\partial Q}{\partial \sigma_{ij}^{\text{eff}}} = \frac{3}{2Q} \left(\sigma_{ij}^{\text{eff}} - \frac{1}{3} \sigma_{kk}^{\text{eff}} \delta_{ij} \right), \tag{19}$$

with δ_{ij} being the Kronecker delta and σ_{kk}^{eff} the trace of the stress tensor. From this, the strain rates along the principal vertical and horizontal directions are:

$$\begin{split} \dot{\varepsilon}_{v}^{i} &= \Lambda \left(\frac{\partial P^{*}}{\partial Q} - \frac{1}{3} \frac{\partial P^{*}}{\partial P} \right), \\ \dot{\varepsilon}_{h}^{i} &= \Lambda \left(-\frac{1}{2} \frac{\partial P^{*}}{\partial Q} - \frac{1}{3} \frac{\partial P^{*}}{\partial P} \right). \end{split} \tag{20}$$

4.2 Horizontal stress in an elastic-viscoplastic thin sheet

We can now follow two approaches to find the expression for the horizontal stress rate:

- (i) We assume that the volumetric inelastic strain rate $\dot{\varepsilon}_{\rm V}^i$ is proportional to the 1-D inelastic strain rate $\dot{\varepsilon}_{\rm 1D}^i$ from a given 1-D subsidence model (Vermeer & Neher 1999).
- (ii) The vertical inelastic strain rate $\dot{\varepsilon}_{v}^{i}$ is equal to the 1-D inelastic strain rate $\dot{\varepsilon}_{1D}^{i}$ from a given 1-D subsidence model.

Note that, under the thin sheet model assumption of uniaxial strain, the volumetric inelastic strain rate is not necessarily equal to the 1-D vertical inelastic strain rate: The sum of elastic and inelastic horizontal strain rates are zero, thus the inelastic horizontal strain

rate that contributes to the volumetric inelastic strain rate can be nonzero. Hence, the first approach assumes *proportionality* between volumetric strain rate and 1-D strain rate. It therefore attempts to reformulate the 1-D elastic-viscoplastic compaction model to a general 3-D compaction model with the same inelastic behaviour in all directions. Such a 3-D model may be used in, for example, finite element software packages. The 1-D model's vertical 1-D stresses and strains, and their rates, need to be expressed in terms of the stress- and strain invariants. Moreover, model parameters of the 1-D compaction model, such as a uniaxial compaction coefficient, need to be redefined to a generic 3-D definition. Hence, recovering the original vertical compaction results from the 1-D model with the adjusted 3-D compaction model requires a full recalibration of the model parameters, in addition to calibration of extra model parameters.

The second approach treats the 1-D elastic-viscoplastic compaction model as a given, without attempting to reformulate it. Previously calibrated model parameters thus remain applicable. Typically, 1-D compaction models are derived from data obtained during oedometer experiments and from surface subsidence. Both these cases have uniaxial strain boundary conditions, which matches with the restriction we impose on the thin sheet model. This approach therefore does not rely on the strong assumption of the first approach.

We elect the second approach: A full 3-D revision of a 1-D compaction model falls outside of the scope of this work, whereas the second approach remains closest to the observed compaction (parametrized by some 1-D model). In addition, we can delay defining a specific 1-D compaction model for another few steps in the thin sheet derivation, keeping the thin sheet formulation a general framework for a variety of 1-D models.

Setting vertical inelastic strain rate equal to the 1-D inelastic strain rate, using eq. (20), the scalar Λ is given as

$$\Lambda = \left[\frac{\partial P^*}{\partial Q} - \frac{1}{3} \frac{\partial P^*}{\partial P} \right]^{-1} \dot{\varepsilon}_{1D}^i, \tag{21}$$

which can be substituted in (20) to obtain the strain rates. Note that up to this point the framework remains general in that no specific 1-D model compaction model and yield function have been adopted, nor have any strain or stress boundary conditions been applied.

Applying now the uniaxial strain boundary conditions (eq. 16) to the sum of the elastic (eq. 6) and inelastic (eq. 20) strain rates, we obtain the effective horizontal stress rate as

$$\dot{\sigma}_{h}^{eff} = \alpha \dot{p}_{f} \frac{\nu}{1 - \nu} + \dot{\varepsilon}_{ID}^{i} \left(\frac{\frac{1}{2} \frac{\partial P^{*}}{\partial Q} + \frac{1}{3} \frac{\partial P^{*}}{\partial P}}{\frac{\partial P}{\partial Q} - \frac{1}{3} \frac{\partial P^{*}}{\partial P}} \right) \frac{E}{1 - \nu}, \tag{22}$$

The partial derivatives can be found by adopting a certain formulation for the yield function f (see Section 4.3).

Next, we may incorporate the known lateral variations in poroelastic moduli, similar to the substitution done for the elastic thin sheet model (eqs 7 and 10). The effect of lateral variations in bulk modulus shall be applied only to the elastic components of eq. (22); we assume that the effect of lateral variations in inelastic behaviour is already captured and calibrated in the 1-D inelastic strain rate function $\dot{\varepsilon}_{1D}^i$. We rewrite eq. (6) as:

$$\alpha \dot{p}_{\rm f} = 2\nu \dot{\sigma}_{\rm h}^{\rm eff} + E \dot{\varepsilon}_{\rm v}^{\rm e}. \tag{23}$$

Young's modulus can be rewritten in terms of uniaxial compaction modulus and Poisson's ratio (Fjaer *et al.* 2008):

$$E = H \frac{(1+\nu)(1-2\nu)}{(1-\nu)}.$$
 (24)

Using some algebra on eqs (22) to (24) give the horizontal effective stress rate

$$\dot{\sigma}_{h}^{\text{eff}} = \frac{H}{1 - \nu} \left(\dot{\varepsilon}_{v}^{e} \nu + \dot{\varepsilon}_{1D}^{i} \frac{\frac{1}{2} \frac{\partial P^{*}}{\partial Q} + \frac{1}{3} \frac{\partial P^{*}}{\partial P}}{\frac{\partial P^{*}}{\partial Q} - \frac{1}{3} \frac{\partial P^{*}}{\partial P}} \right), \tag{25}$$

and horizontal stress rate

$$\dot{\sigma}_{h} = H \frac{1 - 2\nu}{1 - \nu} \left(\dot{\varepsilon}_{1D}^{i} \frac{\frac{1}{2} \frac{\partial P^{*}}{\partial Q} + \frac{1}{3} \frac{\partial P^{*}}{\partial P}}{\frac{\partial P^{*}}{\partial Q} - \frac{1}{3} \frac{\partial P^{*}}{\partial P}} - \dot{\varepsilon}_{v}^{e} \right). \tag{26}$$

In the remainder of this manuscript, the results of the two equations above are referred to as the elastically heterogeneous results, for the lateral variations in poro-elastic moduli it allows. Eq. (22) gives the elastically homogeneous results, since no lateral variations in poro-elastic moduli were incorporated through parameter H_s , and a spatially constant value of $\alpha = 1$ was adopted.

4.3 Yield function: Cam-clay formulation

Now, to complete the elastic-viscoplastic thin sheet model, we adopt the modified Cam-clay formulation for the yield function f. The Cam-clay formulation describes the yield loci as an ellipse centred on the P-axis that passes through the origin of P-Q space:

$$f = Q^2 - M^2 P(P^* - P) = 0, (27)$$

with M the shape factor for the ellipse axis parallel to the Q-axis. Given this definition, the plastic potential is

$$g = P^* = P + \frac{Q^2}{M^2 P},\tag{28}$$

and the partial derivatives of P^* are

$$\frac{\partial P^*}{\partial P} = 1 - \frac{Q^2}{M^2 P^2}$$

$$\frac{\partial P^*}{\partial Q} = \frac{2Q}{M^2 P}.$$
(29)

These derivatives can be substituted in eq. (22) or (25). For the latter, the full ordinary differential equation (ODE) becomes

$$\dot{\sigma}_{h}^{eff} = \frac{H}{1 - \nu} \left(\dot{\varepsilon}_{v}^{e} \nu + \dot{\varepsilon}_{1D}^{i} \frac{\frac{Q}{M^{2}P} + \frac{1}{3} \left(1 - \frac{Q^{2}}{M^{2}P^{2}} \right)}{\frac{2Q}{M^{2}P} - \frac{1}{3} \left(1 - \frac{Q^{2}}{M^{2}P^{2}} \right)} \right). \tag{30}$$

Recalling eq. (5)

$$P = (\sigma_{\rm v}^{\rm eff} + 2\sigma_{\rm h}^{\rm eff})/3$$

$$Q = \sigma_{\rm v}^{\rm eff} - \sigma_{\rm h}^{\rm eff},$$
(31)

the initial conditions required to solve for the horizontal effective stress are:

$$P_{0} = (\sigma_{v,0}^{\text{eff}} + 2\sigma_{h,0}^{\text{eff}})/3$$

$$Q_{0} = \sigma_{v,0}^{\text{eff}} - \sigma_{h,0}^{\text{eff}}.$$
(32)

4.4 1-D inelastic model: RTiCM

To solve the ODE for the evolution of horizontal effective stress we need to adopt some form for the inelastic strain rate function $\dot{\varepsilon}_{\rm 1D}^i$. The rate type isotach compaction model (RTiCM; De Waal & Smits 1988; Pruiksma *et al.* 2015) was elected for this, as it proves to be the best fitting model to the subsidence data for the Groningen field (van Thienen-Visser *et al.* 2015; van Eijs & van der Wal 2017; NAM 2021) in addition to fitting well with experimental data (de Waal 1986; Pruiksma *et al.* 2015). Another advantage is that the

RTiCM model parameters are already calibrated for the Groningen reservoir, so that these can be used as a given.

The 1-D RTiCM model is founded on the concept of the isotach, which is the stress–strain path corresponding to a certain loading rate. A change in loading rate causes the stress–strain path to converge towards the isotach of the new loading rate. The slope of the isotach at higher loading rate is steeper (i.e. stiffer) than at lower loading rate. The isotachs are assumed linear, its slope being the compaction coefficient $c_{\rm m}$. The steepest isotach corresponds to instantenous loading, the slope being the elastic compaction coefficient $c_{\rm m}^{\rm e}$. The spacing between the isotachs, with respect to a reference isotach described by $c_{\rm m}^{\rm ref}$ at loading rate $\dot{\sigma}^{\rm ref}$, can be expressed as a ratio:

$$\frac{c_{\rm m}}{c^{\rm ref}} = \left(\frac{\dot{\sigma}^{\rm ref}}{\dot{\sigma}}\right)^b,\tag{33}$$

where *b* is some empirical constant. All isotachs intersect at one reference point in stress–strain space. This point is implicitly where the material starts deviating from pure elastic behaviour.

Given the above, the viscoplastic strain rate in the RTiCM is given by this set of equations (Pruiksma *et al.* 2015):

$$\dot{\varepsilon}^{\text{total}} = \dot{\varepsilon}^{\text{e}} + \dot{\varepsilon}^{\text{i}},
\dot{\varepsilon}^{\text{i}} = \dot{\sigma}^{\text{ref}} \left(c_{\text{m}} - c_{\text{m}}^{\text{e}} \right) \left(\frac{c_{\text{m}}}{c_{\text{m}}^{\text{ref}}} \right)^{-1/b},
\dot{\varepsilon}^{\text{e}} = c_{\text{m}}^{\text{e}} \dot{\sigma},
c_{\text{m}} = \frac{\varepsilon^{\text{total}} + \sigma^{\text{ref}} c_{\text{m}}^{\text{ref}}}{\sigma}.$$
(34)

All strains and stresses in these expressions are in the vertical direction in the context of the thin sheet model. The material parameters are calibrated on the Groningen subsidence observations by NAM (2021), for which we have taken the mean posterior values of b=0.021, $f^{\rm e}=0.4$ and $f^{\rm ref}=0.8$, where the latter two are multiplication factors to obtain $c_{\rm m}^{\rm e}$ and $c_{\rm m}^{\rm ref}$ from a spatial compaction coefficient grid $c_{\rm m}$. The state parameter $\dot{\sigma}^{\rm ref}$ is set to $1\times 10^{-4.5}$ (TNO 2013). For the stress at the onset of production $\sigma^{\rm ref}$ we use the initial vertical stress $\sigma_{\rm v,0}$ required to solve the equations of the elastic-viscoplastic stress model.

The reservoir strains calculated according to the parameter values and pressure grid for four locations in the field are shown in Fig. 2. The elastic strains are directly proportional to the pore pressure evolution at those locations, indicating that some locations (roughly the north—west halve of the field) will be subjected to continued pore pressure decrease, and at other locations pore pressures stabilize or increase somewhat. The inelastic strain component, about 20 per cent of total strain, continues to increase at all locations up to 2050.

With $\dot{\epsilon}_{\rm ID}^i$ expressed as the inelastic strain rate in eq. (34), this differential equation can be added to the differential eq. (22) (elastically homogeneous thin sheet) or (25) (elastically heterogeneous thin sheet), and solved numerically.

4.5 Results: stress evolution in an elastic-viscoplastic thin sheet

For initial vertical stress $\sigma_{v,0}$, we used the reservoir depth map (Appendix A) to calculate the overburden stress. Initial effective vertical stress $\sigma_{v,0}^{\rm eff}$ was obtained from this overburden and the preproduction pore pressure, known from the pressure history. The initial horizontal effective stress $\sigma_{h,0}^{\rm eff}$ prior to production is difficult

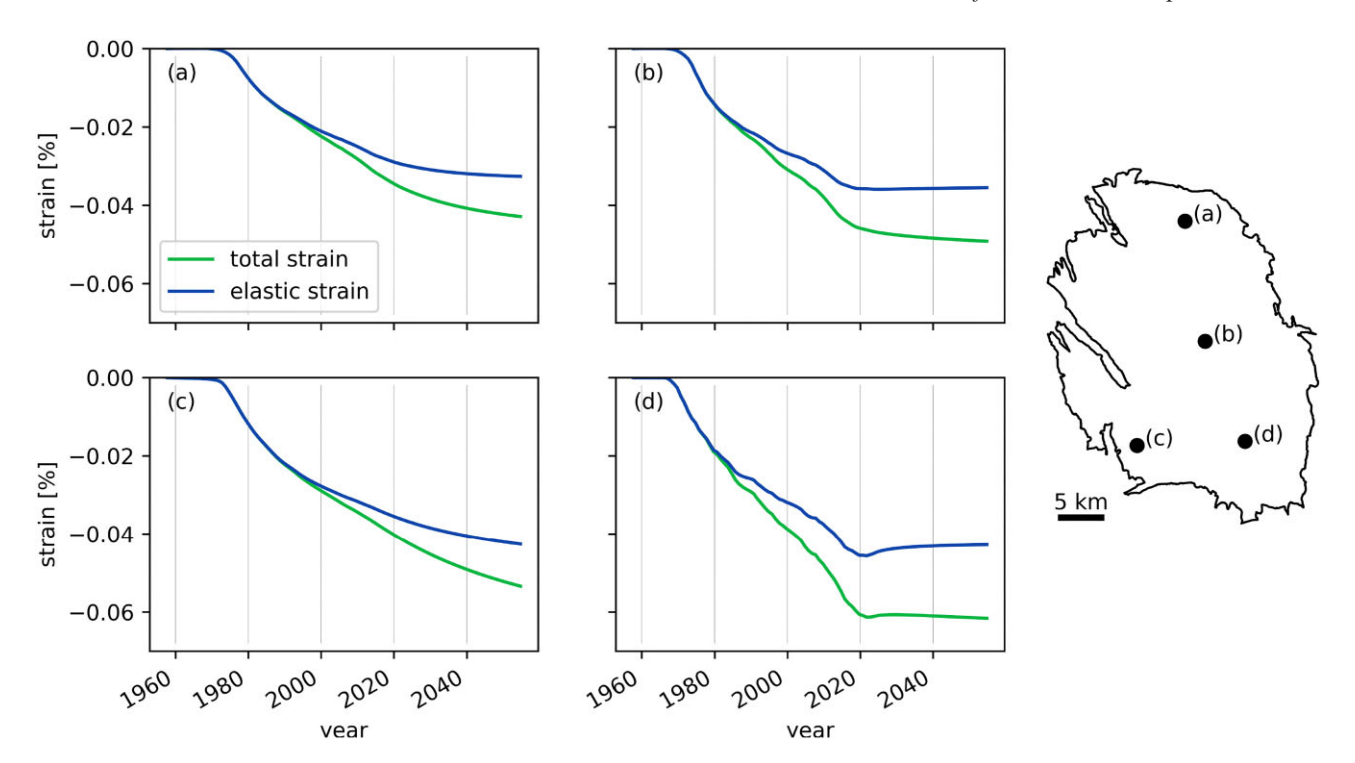


Figure 2. Elastic (blue) and inelastic (green) reservoir strains through time for four locations in the field. Strains are obtained from the Rate Type isotach compaction model and simulated reservoir pressures. The four locations are shown on the reservoir map on the right.

to establish, we therefore treat it as a free parameter in the parameter exploration below. The other free parameters that will be explored are the shape parameter M and the elastic parameter H_s .

We first explore the temporal effect of parameters $\sigma_{h,0}^{\text{eff}}$ and M, by using eq. (22) for an elastically homogeneous thin sheet. Solutions for the horizontal stress were obtained for $\sigma_{\rm h,0}^{\rm eff}=-8$ MPa, $\sigma_{\rm h,0}^{\rm eff}=$ -16 MPa, and a range of values for M (Fig. 3). Focusing on the results for $\sigma_{\rm h,0}^{\rm eff} = -8$ MPa first (Fig. 3a), we see that for M=2the horizontal stress decreases during the shut-in phase. At this phase, where elastic strain is approximately zero given a nearconstant pore pressure, rate-dependent inelastic deformation thus relieves horizontal stresses. At a slightly higher value of $M \approx 2.5$, the elastic-viscoplastic solution yields nearly the same result as the elastic solution. For M > 2.5, the inelastic deformation contributes to a rise in horizontal stress. This contribution increases with increasing M. If a higher initial horizontal stress $\sigma_{h,0}^{\text{eff}}$ is used for the same values of M (Fig. 3b), the normalized stress curves are 'pushed downward', that is, horizontal stress change by inelastic strain during shut-in has a relatively higher contribution to total horizontal stress change. For this initial horizontal stress, the elastic solution is approached at a lower value of $M \approx 2$.

Now we explore parameter H_s that allows for heterogeneous compressibilities. Parameter H_s has a small temporal effect on the total horizontal stress change (Fig. 4, where the curves nearly overlap). The stress curve for a large value of H_s is the same as the stress curve from the elastically homogeneous model (e.g. compare Fig. 4 with Fig. 3a for M=3 and M=4). For $H_s<1\times10^5$ MPa, the viscoplastic contribution to the total horizontal stress change increases slightly. However, the magnitude of the temporal modulation caused by varying H_s , for this particular pressure history and compaction model, is much smaller than the temporal modulation caused by varying M and $\sigma_{h,0}^{\rm eff}$.

We may now focus our attention to the effect of $\sigma_{h,0}^{\text{eff}}$, M, and H_s on the spatial distribution of stress changes. Changing the initial

condition of $\sigma_{h,0}^{\rm eff}$ from -8 MPa to -16 MPa has a very limited impact on the stress distribution of at most a factor 1.2 (Figs 5a and b). Varying the shape parameter M from M=2 to M=4 has more impact on the spatial distribution (Figs 5a and b), although the impact is mainly restricted to the areas where pore pressure decrease is limited. In these areas, near the south-western and northern edges of the reservoir, the normalized stress may be lower by a factor of 1.7 for M=4 compared to M=2. The impact on the other areas is neglible. The impacts of varying M and $\sigma_{h,0}^{\rm eff}$ seems to stem mostly from the spatial variation of initial vertical effective stress that is a function of reservoir depth (Fig. A1). In summary, both parameters do not cause major changes in the spatial stress patterns, except at the edges of the reservoir. The stress pattern is mostly dominated by the spatial distribution of pressure (1b), as is expected for the thin sheet model that does not allow for spatially varying elastic moduli.

The introduction of parameter $H_{\rm s}$ in the spatially heterogeneous formulation of the elastic-viscoplastic thin sheet model modulates the spatial stress pattern (Fig. 6). For a small value of $H_{\rm s}=1\times 10^3$ MPa (Fig. 6a), the pattern mimics the pattern of the elastic compression coefficient grid (Fig. 1a). For a large value of $H_{\rm s}=1\times 10^5$ MPa (Fig. 6b), the pattern reverts to the elastically homogeneous thin sheet model outcome and mimics the spatial pattern of the pressure map (Fig. 1b). The spatial modulation of the stress by parameter $H_{\rm s}$ is by design and identical to the original thin sheet model (Figs 1c and d).

4.6 Simplifications to the model

The model as presented may be calibrated by Bayesian inference on the seismicity data. In this section, we wish to adjust the model in two ways:

(i) We desire that the augmented elastic-viscoplastic thin sheet model can reproduce the exact same results as the original elastic

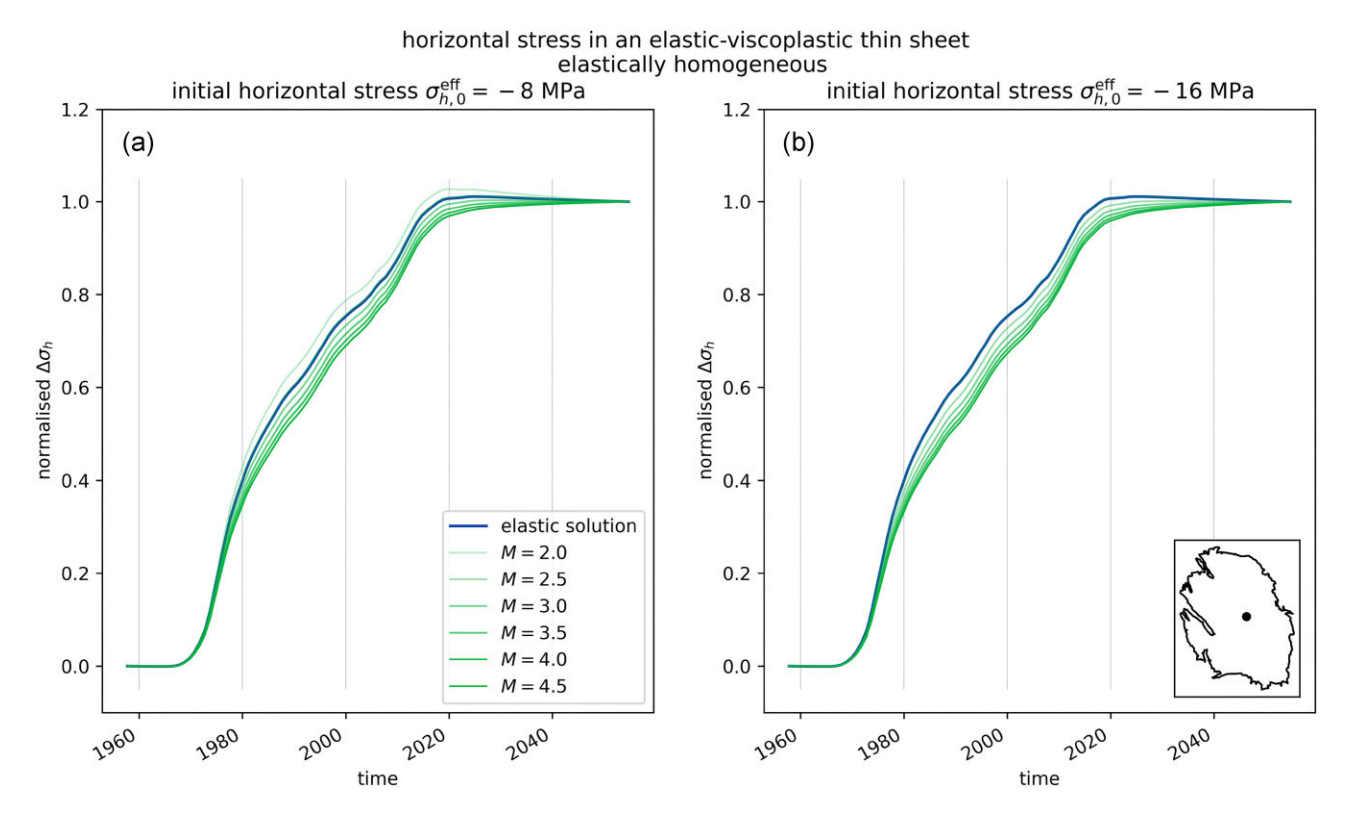


Figure 3. Normalized horizontal stress curves resulting from the elastically homogeneous thin sheet formulation, for an initial horizontal stress of 8 MPa (a) and 16 MPa (b). The RTiCM 1-D compaction model was adopted for the viscoplastic strain rate. For both panels, *M* was varied between 2.0 and 4.5 (green curves). The stresses are based on the pressure history of a point in the centre of the field (see inset for location). The elastic solution (blue curve) is provided for reference.

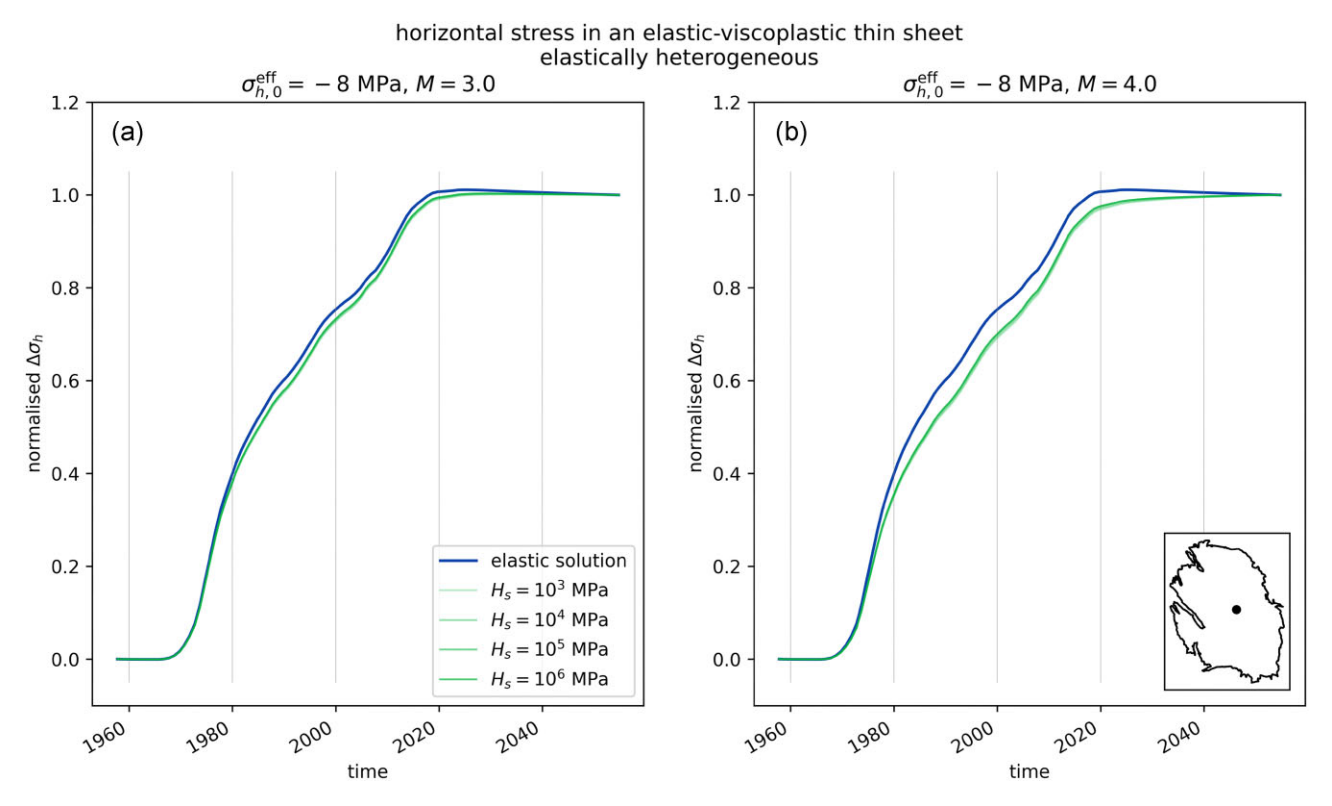


Figure 4. Normalized horizontal stress curves resulting from the elastically heterogeneous thin sheet model for M = 3 (a) and M = 4 (b), and an initial horizontal stress of 8 MPa. The RTiCM 1-D compaction model was adopted for the viscoplastic strain rate. For both panels, H_s was varied over four orders of magnitude.

elastic-viscoplastic thin sheet model elastically homogeneous spatial distribution of horizontal stress increase

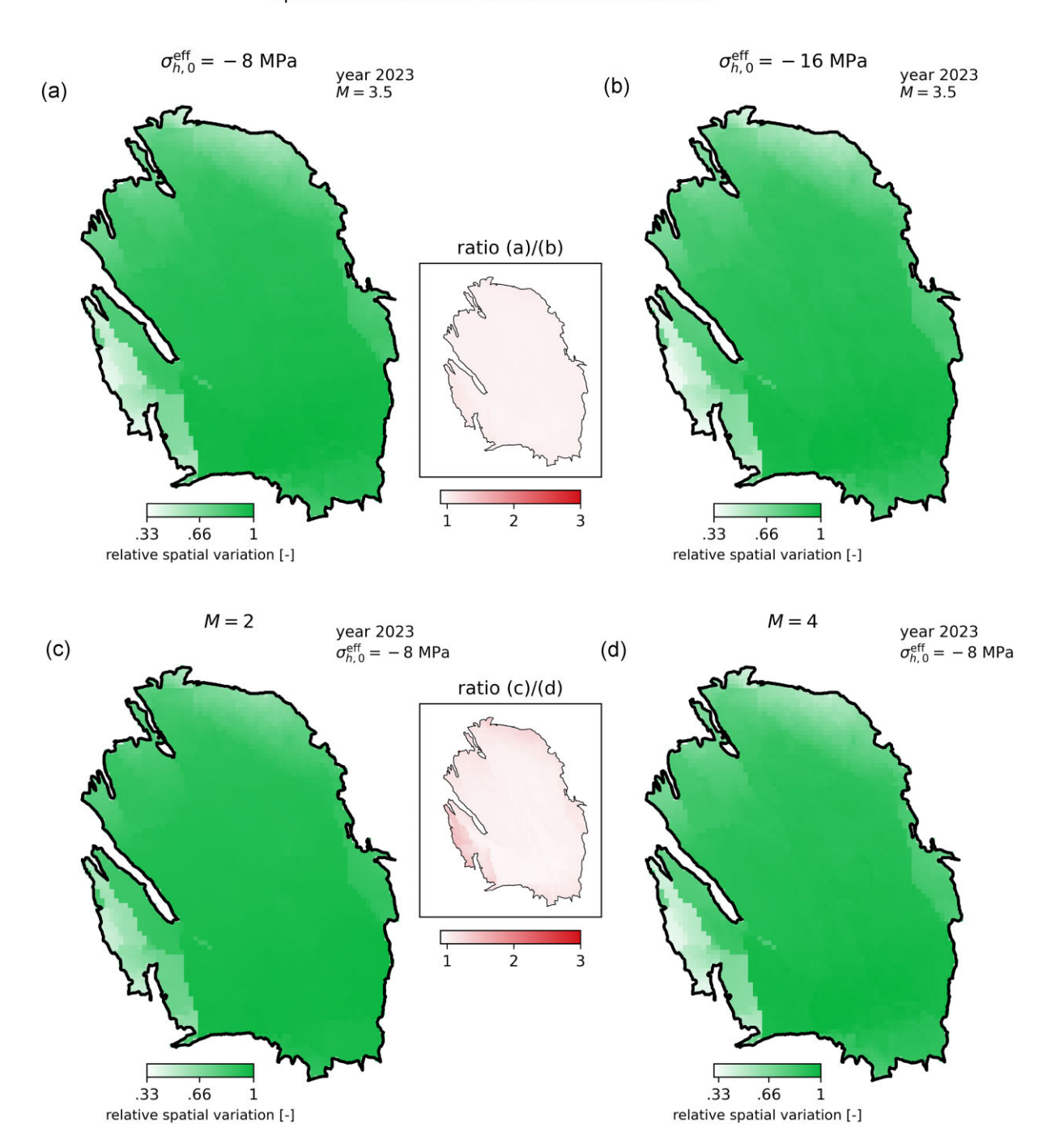


Figure 5. Maps of the Groningen reservoir showing the distribution of horizontal stress resulting from the homogeneous elastic-viscoplastic thin sheet model, for a low (a) and high (b) value of initial horizontal stress $\sigma_{h,0}^{eff}$, and for a small (c) and large (d) value of M, for gas year 2023. Stresses are normalized by the maximum stress in that gas year. Insets: Variations are shown as the normalized stress ratios between panels (a) and (b), and between panels (c) and (d).

thin sheet model. The horizontal stress change over time resulting from the elastic and elastic-viscoplastic models indeed seem to overlap for some combinations of M and $\sigma_{\rm h}^0$ used in the parameter space exploration (Fig. 3): For $(\sigma_{\rm h,0}^{\rm eff}=-8$ MPa, $M\approx2.5)$ and for $(\sigma_{\rm h,0}^{\rm eff}=-16$ MPa, $M\approx2)$. We shall find an analytical solution for this.

(ii) The parameter exploration (Section 4.5) studied the impact of model calibration parameters M, $H_{\rm s}$, and initial condition $\sigma_{\rm h,0}^{\rm eff}$ on the horizontal stress increase. Of these, $H_{\rm s}$ was already present in the elastic thin sheet model, where it modulates the spatial stress pattern (Fig. 1). In the elastic-viscoplastic model, it kept its intended role as strong modulator for the spatial stress distribution (Fig. 6).

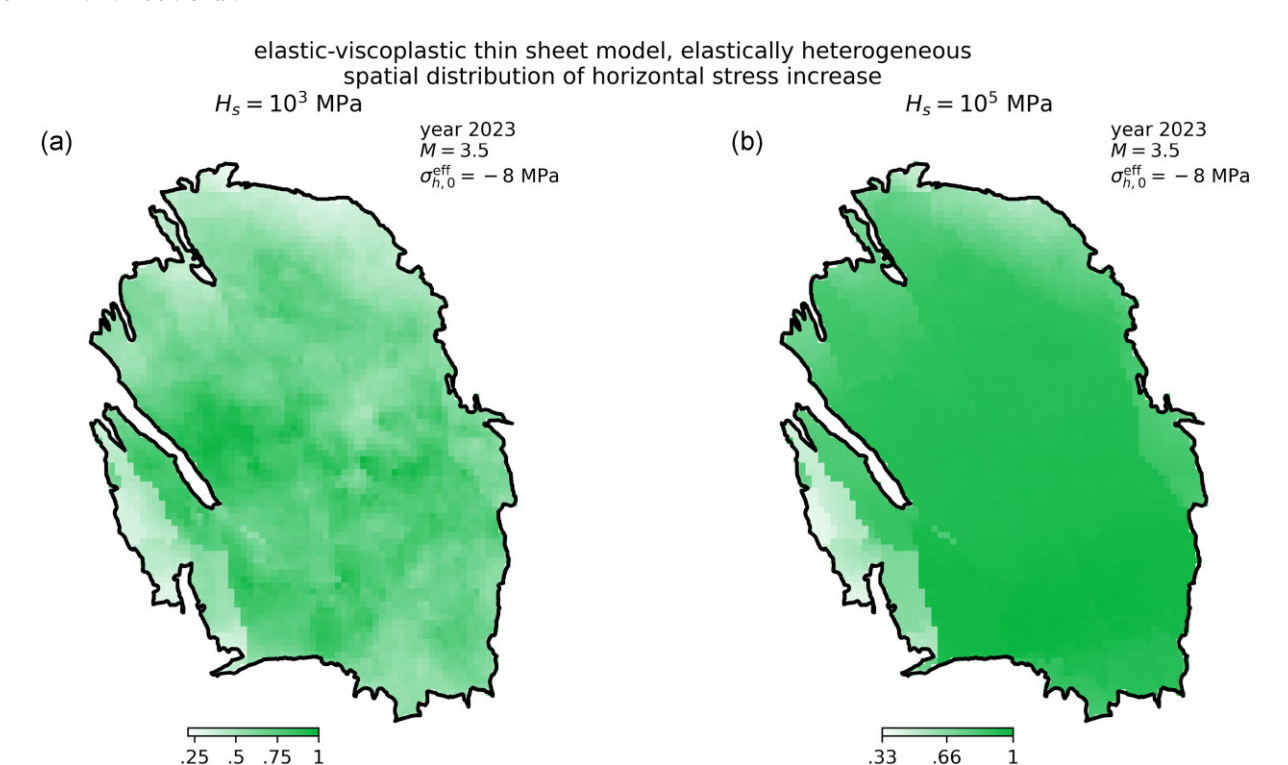


Figure 6. Maps of the Groningen reservoir showing the distribution of horizontal stress resulting from the elastically heterogeneous thin sheet model, for a low (a) and high (b) value of model parameter H_s for gas year 2023. Stresses are normalized by the maximum stress in that gas year. The spatial variations are identical to those in Figs 1(c) and (d).

However, M and $\sigma_{h,0}^{\rm eff}$ have a weak effect on the spatial distribution as well (Fig. 5). Conversely, M and $\sigma_{h,0}^{\rm eff}$ have a strong temporal effect whereas $H_{\rm s}$ has weak effect on the temporal stress history (Figs 3 and 4). The parameter exploration was conditional on a certain choice of compaction model and pressure history; albeit a realistic scenario, the qualitative labels 'strong' and 'weak' modulators may not be generally valid. The model can thus be calibrated with these parameters, but there will be some trade-offs and redundancy between all three parameters for a good spatial and temporal fit to the data. We shall attempt some simplifications of the model, with the intent to obtain model parameters with a less ambiguous effect on the spatio-temporal stress distribution.

relative spatial variation [-]

We start our adjustements of the model by identifying the special case where the elastic and elastic-viscoplastic horizontal stress solutions overlap in time. An analytical solution can be found for this problem (see Appendix B for the full derivation):

$$M^{\text{elastic}} = 3 \begin{pmatrix} \frac{\sigma_{v,0}^{\text{eff}}(1-k_0) + \Delta \sigma_{v}^{\text{eff}}\left(1-\frac{\nu}{1-\nu}\right)}{\sigma_{v,0}^{\text{eff}}(1+2k_0) + \Delta \sigma_{v}^{\text{eff}}\left(1+2\frac{\nu}{1-\nu}\right)} \end{pmatrix}^{2} \\ + \frac{\sigma_{v,0}^{\text{eff}}(1-k_0) + \Delta \sigma_{v}^{\text{eff}}\left(1-\frac{\nu}{1-\nu}\right)}{\sigma_{v,0}^{\text{eff}}(1+2k_0) + \Delta \sigma_{v}^{\text{eff}}\left(1+2\frac{\nu}{1-\nu}\right)} \end{pmatrix}$$
(35)

Here, $k_0 = \sigma_{\rm h,0}^{\rm eff}/\sigma_{\rm v,0}^{\rm eff}$, the ratio of the initial horizontal effective stress over the initial vertical effective stress, also known as the pre-consolidation ratio. Note that here, k_0 is considered an initial condition, the ratio of the horizontal to vertical stress is allowed to change during a loading history. $M^{\rm elastic}$ is the value of M for which elastic behaviour is obtained with the elastic-viscoplastic model. Note that $M^{\rm elastic}$ is independent of $H_{\rm s}$, but contains the vertical effective stress change $\Delta\sigma_{\rm v}^{\rm eff}$. This means that the value of $M^{\rm elastic}$ may change with vertical load, that is, $M^{\rm elastic}$ is not necessarily

constant throughout a pressure history (Fig. 7). This is impractical for Bayesian inference of model parameter M, where the elastic solution is desired as one of the possible outcomes. Whether $M^{\rm elastic}$ is constant depends on the choice of k_0 (Fig. 7). Indeed, $M^{\rm elastic}$ is constant if k_0 is equal to the term containing the Poisson's ratio, $\frac{\nu}{1-\nu}$, so that eq. (35) simplifies to:

relative spatial variation [-]

$$M^{\text{elastic}} = 3\sqrt{\left(\frac{1 - \frac{\nu}{1 - \nu}}{1 + \frac{2\nu}{1 - \nu}}\right)^2 + \frac{1 - \frac{\nu}{1 - \nu}}{1 + \frac{2\nu}{1 - \nu}}}$$
(36)

For instance, for $\nu=0.2$ we obtain $M^{\rm elastic}\approx 2.598$. The implications for setting $k_0=\frac{\nu}{1-\nu}$, also known as the bilateral constraint (Eaton 1969; Zoback 2010), will be discussed later. Eq. (36) shows that the elastic thin sheet solution of Bourne & Oates (2017) can be recovered for $M^{\rm elastic}$, who's value depends on the choice of Poisson's ratio.

We can now attempt to remove the initial condition model parameter $\sigma_{h,0}^{\rm eff}$ (or equivalently k_0), which has a similar temporal effect on stress change as M, and is therefore considered redundant. Lacking knowledge on the initial horizontal stress and its spatial distribution prior to production, we followed the assumption of a spatially constant initial horizontal stress $\sigma_{h,0}^{\rm eff}$ in the parameter exploration. An alternative assumption is that of a spatially constant initial stress ratio k_0 . The initial values for P and Q (eq. 5) then become:

$$P_0 = \frac{\sigma_{\text{v},0}^{\text{eff}}}{3} (1 + k_0)$$

$$Q_0 = \sigma_{\text{v},0}^{\text{eff}} (1 - k_0).$$
(37)

With these new initial conditions, the ODEs for the elastic-viscoplastic model can be solved again for varying values of k_0 and M. Varying k_0 has the same temporal effect to varying $\sigma_{\rm h,0}^{\rm eff}$.

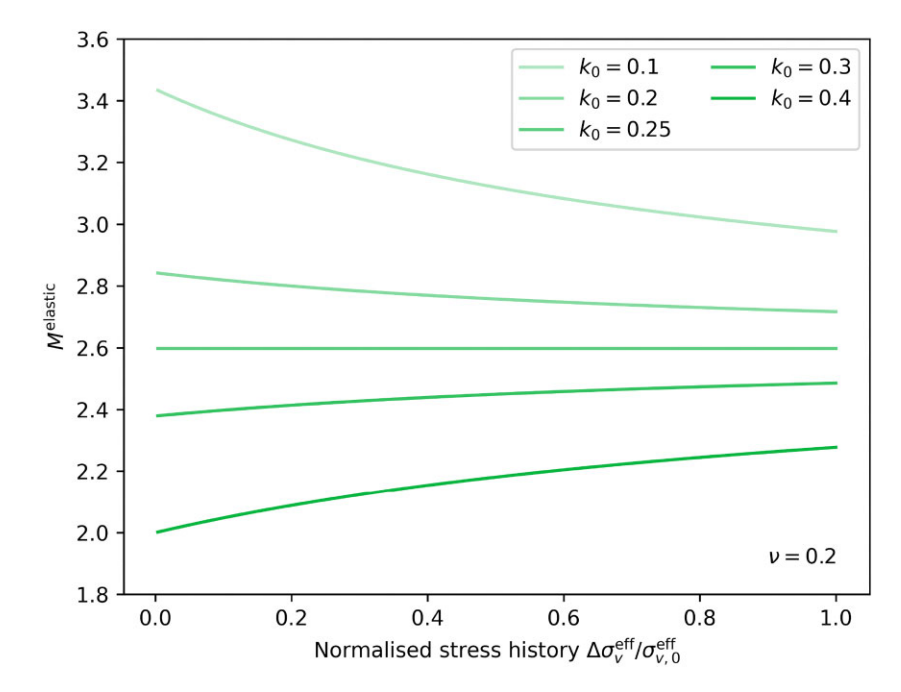


Figure 7. Normalized vertical stress (defined as $\Delta \sigma_{\rm v}^{\rm eff}/\sigma_{\rm v,0}^{\rm eff}$) versus $M^{\rm elastic}$, for different values of k_0 .

However, if we want to include the exact elastic thin sheet solution for constant $M^{\rm elastic}$ through time as a possibility in the elastic-viscoplastic model, k_0 has to equal $\frac{\nu}{1-\nu}$, and initial stress conditions become:

$$P_0 = \frac{\sigma_{v,0}^{\text{eff}}}{3} \left(1 + \frac{\nu}{1 - \nu} \right)$$

$$Q_0 = \sigma_{v,0}^{\text{eff}} \left(1 - \frac{\nu}{1 - \nu} \right),$$
(38)

eliminating $\sigma_{h,0}^{\text{eff}}$ (or equivalently k_0). Now, M remains as the main temporal modulator of the stress change (Fig. 8a), and H_s has only a minor impact on temporal stress evolution (Fig. 8b).

The imposed bilateral constraint $(k_0 = \frac{\nu}{1-\nu})$ (Eaton 1969; Zoback 2010) merits some discussion. The bilateral constraint assumes that the horizontal stress depends solely on the load of the overburden through the Poisson expansion effect, implying that no tectonic stresses are imposed on the system. We are aware that this simple relation fails to reproduce most in situ stress measurements, even in tectonically quiet areas, and is therefore generally considered 'unwise' to use (for discussion, see section 9 in Zoback 2010). However, in the context of the presented model and its intended application, we feel that this assumption is not detrimental: As shown above, the assumption simplifies the model, removes redundancy between model parameters, and ensures that the linear elastic solution can be included for a constant value of M given by eq. (36). The absolute values of stress and stress change are affected by the choice of k_0 . However, in the context of a seismic source model, we are not interested in absolute stresses or stress changes-typically, the stress amplitudes put into an activity rate model are rescaled by some model parameter. It is the shape of the curve describing the stress change over time that matters. As can be seen by comparing the normalized solutions in Fig. 8 with those in Figs 3 and 4, the simplified solution can cover the solutions of the full model. We can therefore justify this simplification of the model in this specific context of applying it in a seismic activity rate model.

Finally, in our model, the horizontal stress increase for a unit of inelastic strain is a function of stress itself (i.e. hence the ordinary differential equation), except in two cases: (i) where a unit of inelastic strain has no impact on horizontal stress as presented above, and (ii) where a unit of inelastic strain causes the same increase in stress as a unit of elastic strain (Fig. 8, grey curve). This second case is achieved for $M \to \infty$, so that the elastic and inelastic strain rates in eq. (26) are multiplied by the same elastic term. The normalized stress space between these two boundaries (the elastic solution and the solution with maximum inelastic impact on stress) can be populated by stress histories by varying M, but equidistant curves in stress do not scale linearly with M.

5 DISCUSSION

We formulated an elastic-viscoplastic stress model as an expansion of the elastic thin sheet stress model of Bourne & Oates (2017). This was done to achieve consistency in reservoir behaviour between the seismic source model, field-scale subsidence models and observations, and laboratory studies. To use calibrated 1-D subsidence models to obtain a 3-D state of stress requires the additional model parameter M. We further show that the original model parameter H_s has retained the same functionality as in the elastic thin sheet model of Bourne & Oates (2017), as intended.

Parameter M parametrizes the change in horizontal stress for a given amount of inelastic vertical strain, depending on the state of stress. 1-D subsidence models, such as the RTiCM, can emperically capture spatio-temporal variations for inelastic vertical strain, but they cannot, by definition, capture the impact of vertical inelastic strain on horizontal stress change, that is, M cannot be determined from subsidence data. In the absence of regular $in\ situ$ horizontal stress measurements, constraints on M on the scale of the reservoir must be derived from horizontal stress proxies—for instance, earthquake events. In the following section, we will indeed calibrate M using seismicity from the Groningen field.

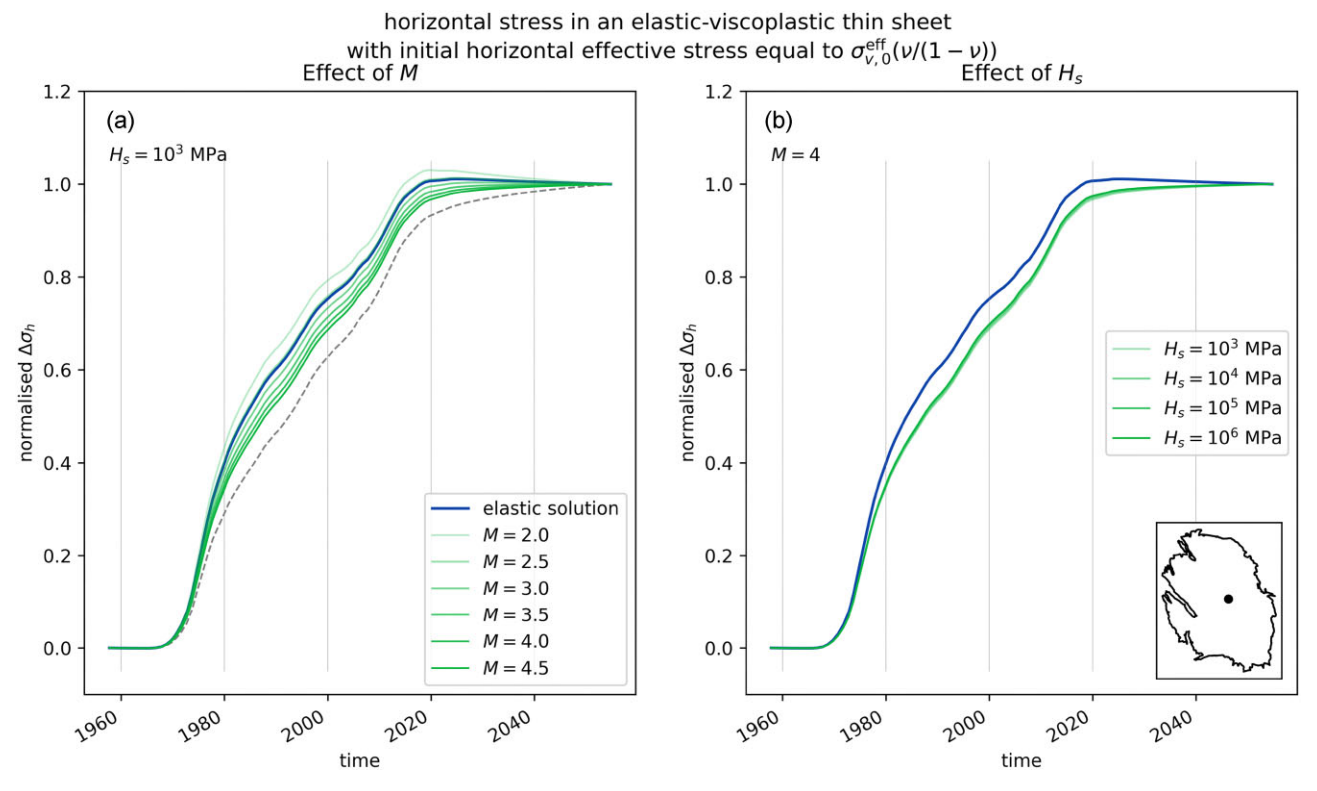


Figure 8. Normalized horizontal stress curves resulting from the simplified elastic-viscoplastic thin sheet formulation, assuming $k_0 = \frac{\nu}{1-\nu}$. (a) Effect of parameter M on the stress evolution. (b) Effect of parameter H_s on the stress evolution. The stresses are based on the pressure history of a point in the centre of the field (see inset for location). The elastic solution (blue curve) and stress solution with optimal impact of inelastic strain (for $M \to \infty$ grey dashed curve) are provided for reference.

We note that the impact of inelastic vertical compaction on the horizontal stress is determined by the micromechanical processes underlying inelastic behaviour, as shown by laboratory experiments on Groningen reservoir rock or its analogue (e.g. Pijnenburg $et\ al.$ 2019; Hangx & Pijnenburg 2023; Shinohara $et\ al.$ 2024). The inelastic strain contributions of these processes may vary as a function of stress, strain and rock properties (e.g. porosity, clay content). In other words, the horizontal stress increase for a given amount of inelastic vertical strain may change spatially and with time. Conceptually, this could be represented in our model by a spatially or temporally varying value for M. However, to justify such variations of M at the reservoir scale requires upscaling of the current physical understanding of these micromechanisms (Shinohara 2024). For now, in our implementation, M remains spatially and temporally constant.

5.1 Application to forecasting seismicity in Groningen

5.1.1 Approach

In this section the performance of the newly developed stress model for seismicity modelling is assessed relative to the original elastic thin sheet stress model by analysing pseudo-prospective forecast results. To do so, the elastic-viscoplastic thin sheet stress model was implemented in the seismic source model used for the public SHRA for Groningen performed by TNO Geological Survey of the Netherlands on behalf of the Dutch Government (TNO 2023, for the latest edition). The seismic source model produces event rates as a function of location, time and magnitude, and is comprised of the following components:

- (i) Stress model: either the elastic thin sheet stress model (Bourne & Oates 2017) or the elastic-viscoplastic thin sheet stress model presented here.
- (ii) Activity rate model: extreme threshold failure model (Bourne & Oates 2017).
- (iii) Aftershock model: ETAS model (Ogata 2011; Bourne *et al.* 2018).
- (iv) Magnitude–frequency model: Reservoir thickness was chosen as the predictor for the Gutenberg–Richter b-value (Kraaijpoel et al. 2022). Gutenberg–Richter relations were truncated by the logic tree for the maximum magnitude $M_{\rm max}$ (Coppersmith et al. 2022).

The input data for the seismic source model has been described in Section 2.2, with the only difference being the compaction coefficient grids: For the elastic-viscoplastic model, the calibrated RTiCM model including elastic compaction coefficient grid of NAM (2021) is used. For the elastic model, a compaction coefficient grid is used derived from an elastic subsidence inversion (Bourne *et al.* 2018).

The seismic source model has the model parameter vector:

$$\theta = \{\underbrace{H_{\rm s}, M, r_{\rm max}, L_{\rm s}}_{\text{stress model}}, \underbrace{\theta_0, \theta_1}_{\text{activity rate model}}, \underbrace{a, K,}_{\text{ETAS}} \underbrace{b_{\rm low}, b_{\rm high}, d_{\rm split}}_{\text{MF model}}\}. \tag{39}$$

Here, $r_{\rm max}$ is a parameter in the stress model that filters the total set of available faults considered for the stress amplification factor, based on a maximum allowable local throw-to-thickness ratio (Bourne *et al.* 2018). $L_{\rm s}$ is a stress smoothing lenght-scale that represents spatial uncertainties (e.g. fault- and event locations, Bourne & Oates 2017). For the meaning of the other parameters we refer to the references listed at the model components above. The subsidence

model parameters can be included in this vector if one intends to add the subsidence model to the forward model workflow. We elect to use the calibrated mean RTiCM parameter values from NAM (2021), noting that their uncertainties are relative narrow and that the shape of the inelastic strain history curve does not change, merely its magnitude relative to the elastic strain component. Hence, we infer that such a relative change would be 'compensated' by parameter M in the stress model.

The N observed events $X=(X_1,...X_N)$ are characterized by origin time, epicentral location and magnitude, and were obtained from the earthquake event catalogue of the KNMI (Royal Dutch Metreological Institute). We assume that X stems from the rate model $\lambda(X|\theta)$. The posterior model parameter probabilities $p(\theta|X)$ are obtained from Bayesian inference with a parameter grid evaluation method, and are then used for forecasting seismicity rates. Uniform prior distributions were used for all parameters. The parameter ranges were iteratively adapted until the bulk of the posterior probability was well included within the parameter grid space for all parameters except M.

The uniform prior for M is set between M=2 and M=5.5 with steps of 0.5, thus giving the possibility for inelastic strain to reduce stress at low M and to augment stress for larger M. The elastic solution at $M\approx 2.598$ falls within the prior range. Stress solutions for increasingly larger M converge towards the solution with maximum inelastic impact on stress (Fig. 8), with less differences in stress between solutions per unit M. We have therefore set an upper limit on the prior range of M=5.5, where reasonably large differences between stress solutions start to disappear.

The two models were calibrated on a catalogue ranging from 1995 January 1 to 2020 December 31, with a minimum magnitude of $M_{\rm min}=1.5$. Event rates were forecasted between the 2021 January 1 and 2024 December 31 (i.e. the testing period) and hind-casted over the calibration period. We only considered the testing period for the performance of the two models, which is expressed as the log-likelihood of the modelled rates given the observed events (Schorlemmer *et al.* 2007):

$$ll = +\sum_{k=1}^{N} -\Lambda_k \ln(\lambda_k), \tag{40}$$

where λ_k is the modelled rate at the location and time interval of observed event k, and Λ_k the integral of the modelled rates over the entire space domain and the time interval of event k. The time interval for each event is half the interevent time with the preceding event and half the interevent time with the next event in the catalogue. We did not consider event magnitudes in this test, since the magnitude–frequency model is the same for both models.

5.1.2 Results

We obtained posterior parameter distributions for both the elastic and the elastic-viscoplastic models (see Figures C1 and C2 in Appendix C), conditional on the training data set. The marginal posteriors of most parameters are well-bounded, except for M in the elastic-viscoplastic model posterior. Here, values of M > 3.0 seem to be preferred, indicating that the elastic solution (at $M \approx 2.598$) is not the optimal one and an additional stress contribution from inelastic compaction improves the fit. Values for M < 2.598 carry neglible probability, rejecting stress reduction by inelastic processes. The

posterior distribution seems to saturate at M > 3.0 up to the arbitrarily chosen upper limit of M = 5.5, indicating that the data cannot distinguish between these various amounts of additional stress by inelastic compaction. We thus recognize that the choice of prior impacts the final results. This problem may be alleviated by a different parametrization of the prior of M, and most importantly, by using better constraints on the range of M based on, for instance, experiments.

In the testing period, the modelled field-wide event counts and its prediction intervals given by the elastic model seem to underpredict the observed counts: 25 events were modelled versus 38 observed, and the observed counts regularly fall near or on the upper bound of the modelled prediction interval (Fig. 9, left panel). The elastic-viscoplastic model fits better with the observed counts (35 modelled events), with all years in the testing period well within the modelled prediction interval (Fig. 9, left panel). In the training period, the differences are less clear-cut: The systematic overestimation of the modelled expectaction values in the period 2012–2015 is somewhat larger for the elastic model, but drops faster towards observed values. However, the observed counts fall well within the prediction intervals of both models.

The model improvement visible in the total event count plots is indeed confirmed by assessing the log-likelihood scores of the models' spatio-temporal performance. These scores clearly indicate that the elastic-viscoplastic stress model (Il=-321.8) performs better than the elastic model (Il=-32.5). The large log-likelihood difference between the two models invites further analysis. Log-likelihoods obtained for most of the separate events in- or decrease by a small amount for the elastic-viscoplastic model (Fig. 10). A number of events with log-likelihoods <-10 for the elastic model, mainly located towards the centre and south of the field (Fig. 10a), show the largest increase from elastic to elastic-viscoplastic model (Fig. 10b). Note that one event at the southern edge of the reservoir with a very low likelihood for both models (highlighted by asterisk in Fig. 10) does show the largest increase of $\Delta Il \approx 6.5$.

5.1.3 Interpretation and discussion

The elastic-viscoplastic model outperforms the elastic model. This improvements stems from a better match between the number of forecasted events and the number of observed events, and a better spatial forecast. A higher Coulomb stress change yields a higher rate from the extreme threshold activity model (Bourne & Oates 2017). The Coulomb stress change is larger due to the contribution from inelastic rate-dependent deformation, in addition to the stress increase by pore pressure reduction. This direct pore pressure contribution to the stress increase is fairly low across the field during the testing period due to much lower production rates and shut-in. Even more, a number of events, all observed from 2019 onward, are concurrent with a local pressure increase according to the reservoir model (Fig. 11, four events in the calibration catalogue and three in the testing catalogue) – meaning that at these locations, the Coulomb stress change is actually negative when only considering elastic reservoir behaviour. There, the elastic stress model would not predict event rates at these locations at all, if it were not for the non-zero (but still very low) rates from the ETAS clustering model. The Coulomb stress change in the elastic-viscoplastic stress model can remain positive for sufficiently large values of parameter M, modelling non-zero rates at these locations. Hence, the likelihood gain is largest for these observed testing events that occured concurrently with an increase in pore pressure (Figs 11 and 10b).

event counts

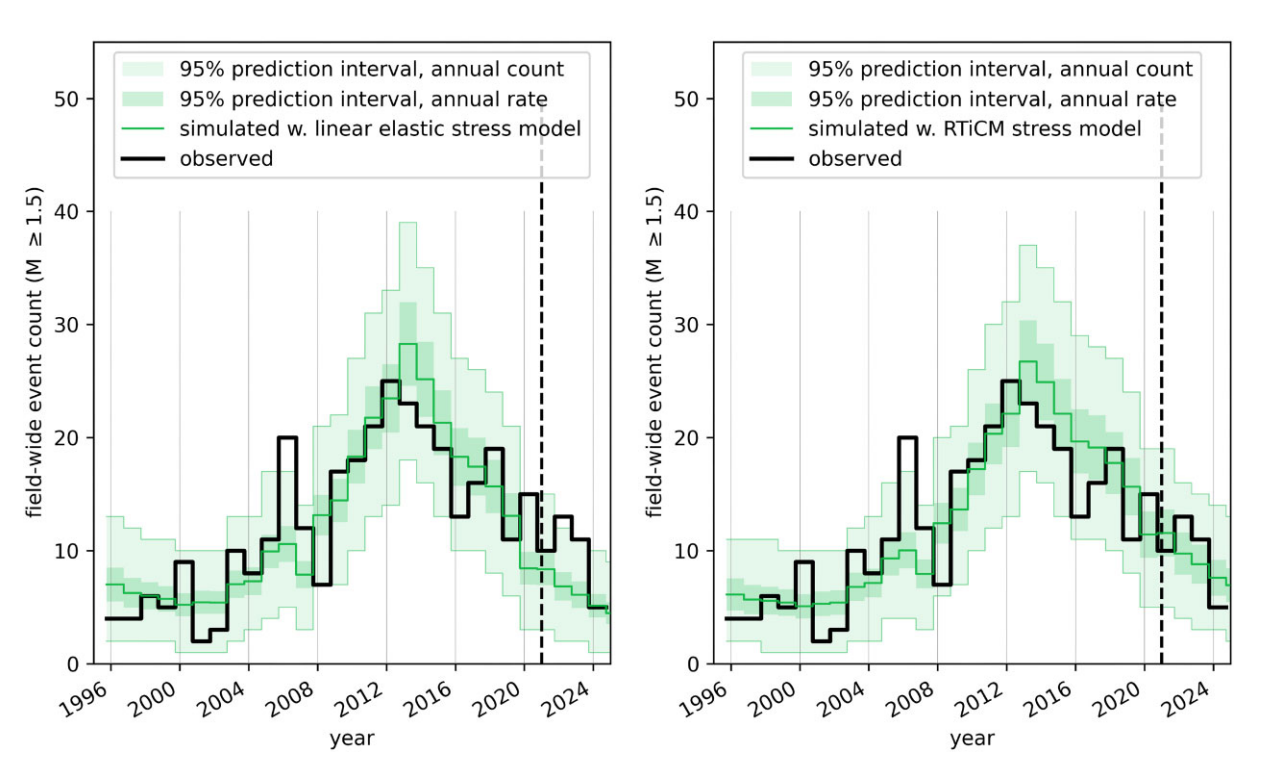


Figure 9. Observed (black curve) field-wide event counts and modelled (green curve) mean event rates for the elastic model by Bourne & Oates (2017) (left panel) and for the elastic-viscoplastic model presented here (right panel), with 95 per cent intervals for the modelled rates (dark green) and modelled counts (light green, for simulated mean rates only). The dashed line indicates the division between calibration and testing periods.

We note that the pressure increase at the seven event localities in Fig. 11 are fairly small, typically about 0.5 bar and only one event with a pressure increase larger than 1 bar (1.6 bar). For the areas where the testing events mostly occur, the root mean square error of the history matched reservoir model pressures with the downhole recorded pressures is around 1.4 bar (see fig. 1 in Landman & Vissers 2023)—an error larger than the small pressure increases. Likely, this error is larger (towards 3 bar) further away from the wells at edges of the reservoir. Similarly, the error of 1.4 bar is larger than the pressure decreases concurrent with 17 out of the 36 events in the testing catalogue. This indicates that pressure variations in the most recent years are small relative to the uncertainty of the reservoir simulation results. Nonetheless, observed events occurred in regions where pressure variations are small and have a possibility of actually increasing.

Continued seismicity after reduction and shut-in of the Groningen field suggest that temporal delay mechanism(s) are required in addition to linear elastic behaviour in order to model the observed spatio-temporal event counts. Here, we have demonstrated that this can be achieved by including inelastic deformation as additional driver for Coulomb stress increase. Other delay mechanisms have been considered in the currently available source models, most notably, the well-known concept of rate-and-state friction (Dieterich 1994). Rate-and-state friction provides a delay between stress and failure, and has been applied to Groningen by some studies (e.g. Candela *et al.* 2019; Richter *et al.* 2020; Heimisson *et al.* 2022). Rate-and-state friction theory is founded on the concept of critically stressed faults. If the Groningen reservoir faults are indeed close to criticality from the onset, the decades-long delay between

start of production and seismicity implies a very long response time (Candela *et al.* 2019). This long response time results in a delayed decline of seismicity rates, thus in a large overestimation of the observed event count in recent years (see e.g. fig. 6b in Heimisson *et al.* 2022).

A recent iteration of the rate-and-state model by Heimisson et al. (2022) attempts to correct this issue by incorporating a Coulomb stress threshold in the rate-and-state framework. The stress threshold represents the assumption that the faults in the reservoir are not critically stressed at the onset of production (Van Wees et al. 2014; Bourne & Oates 2017). Motivated by the apparent success, we have implemented this Coulomb stress threshold rate-and-state model, and, combined with the elastic thin sheet stress model, applied the calibration procedure to it. The obtained results were unsatisfying: The rate-and-state solution with a long response time and a very low stress threshold provided the only feasible fit-effectively reverting back to the original Dieterich (1994)-model (see Appendix D), whereas Heimisson et al. (2022) found a much higher stress threshold and shorter response time. Although we have used a different stress model compared to Heimisson et al. (2022) (but both founded on poro-elasticity), we believe the source of this discrepancy lies in the calibration procedure rather than the particularities of the stress model: Whereas we utilized a fully spatio-temporal likelihood function, Heimisson et al. (2022) (and subsequent publications e.g. Acosta et al. 2023; Kaveh et al. 2024) utilized a temporal likelihood function. The latter approach results in physical inconsistency, as the stress threshold can be calibrated to a higher value than stresses at observed event locations, as long as the model predicts sufficient events elsewhere in the field to match the total observed events (see

elastic model elastic-viscoplastic model (a) Poogujayii-bo 1 -11 5 km

log-likelihood, per event

Change in likelihood (II_{plastic} - II_{elastic}) (b) 2.5 0.0 5 10 15 20 25 30 35 event index

Figure 10. (a) Event locations in the testing period, marker colours providing the log-likelihood values for the elastic model (left) and elastic-viscoplastic model (right). (b) Log-likelihood difference between plastic and elastic model per event, positive change indicating a gain in likelihood for the elastic-viscoplastic model. Marker colours are absolute log-likelihood values for the elastic model. Arrows indicate events that occurred concurrently with pressure increase (see Fig. 11). Asterisk in both panels: Event with log-likelihood lower than colourbar minimum of -12 (ll = -20.4 and ll = -13.9 for elastic and elastic-viscoplastic model, respectively).

Appendix D for a more elaborate illustration of this issue). Hence, the concept of rate-and-state friction is not yet successfully applied in seismic source models for Groningen.

Another delay mechanism are aftershocks. Here, they have been considered through the statistical ETAS model (Ogata 2011) as part of the seismic source model (Bourne *et al.* 2018). The ETAS model can explain the pressure increase-concurrent events, albeit with a very small likelihood—orders of magnitude smaller than for events in areas of pressure increase, as well as order of magnitude smaller than the likelihood given by allowing for stress increase by inelastic deformation (Fig. 10). Rate-and-state failure and aftershocks are both scientifically reasonable mechanisms, however their current implementations combined with linear elastic reservoir deformation only cannot explain the observed events in a convincing manner.

6 CONCLUSION

We have presented a 3-D stress—strain framework that is able to house 1-D non-linear stress—strain relations typically used for subsidence models, without the need for recalibration of the subsidence model parameters. The framework is based on the formality of critical state mechanics for porous media. The generic framework was implemented in the elastic thin sheet stress model of Bourne & Oates (2017) that is part of the seismic source model for induced

seismicity forecasts and hazard and risk analysis in the Groningen gas reservoir. For Groningen, the Rate-Type isotach compaction model as calibrated by NAM (2021) was adopted as a non-linear 1-D model, but any other 1-D subsidence model that expresses total strain as the sum of elastic and inelastic strains may be chosen. By doing so, we have allowed for mechanical reservoir behaviour that is consistent with subsidence observations, and that incorporates phenomenologically the mechanical behaviour seen in laboratory experiments. Relative to linear poro-elastic reservoir behaviour, the augmented thin sheet stress model may have additional fault stressing caused by inelastic deformation. The stress contribution from inelastic deformation is shown to be modulated by the critical state line model parameter M. For a specific value of M, the model reverts to the original elastic thin sheet stress model. We also showed that other model parameters maintained their functionality as intended in the original elastic stress model.

The performance of the new elastic-viscoplastic thin sheet stress model for seismicity forecasting was assessed relative the original elastic model with a pseudo-prospective forecast, after calibrating the model parameters in a probabilistic Bayesian approach. We showed that including rate-dependent inelastic deformation obtained from subsidence observations greatly improves model performance over a 4 yr period between 2021 and 2025, by a likelihood increase of nearly five orders of magnitude. Compared to the model based on linear elasticity, the testing catalogue was better explained

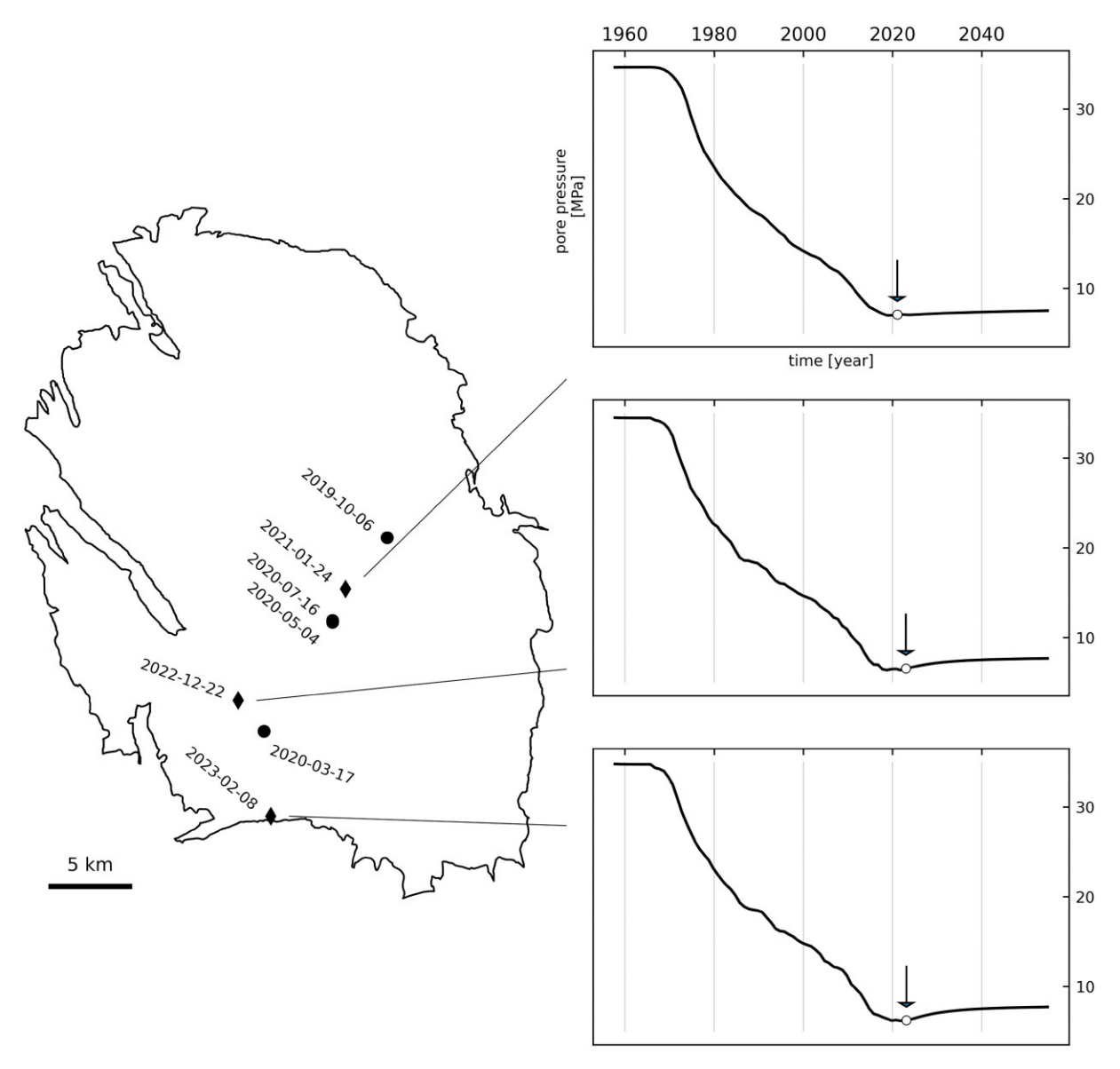


Figure 11. Locations of events that occurred concurrently with pressure increase (according to the reservoir model) in the Groningen reservoir plotted onto the contour of the reservoir. The event time is provided for each event. Circles: events in the calibration catalogue. Diamonds: events in the testing catalogue. Note that the markers for events at 2020 July 16 and 2020 May 04 nearly overlap. Insets: pore pressure history and forecast for the three pressure-increase concurrent events in the testing catalogue. The arrows indicate the event occurrence in the pressure time-series.

by the model which includes elasto-viscoplasticity. This improvement is most pronounced for the small number of events that were concurrent with a pressure increase, that is, a stress decrease away from failure in the case of linear elastic reservoir behaviour, due to the additional stress increase by inelastic deformation. Notwith-standing uncertainties on the pressure data, we showed that our improved stress model is well suited to explain seismicity in a reservoir with stabilizing pressures, such as the Groningen gas field in its post shut-in phase.

ACKNOWLEDGMENTS

We thank Jaap Breunesse and Hans de Waal for insightful discussions and NAM, in particular Rob van Eijs, for sharing their work on subsidence inversion results.

DATA AVAILABILITY

Figures are based on data available at Zenodo (2023) (https://doi.org/10.5281/zenodo.10245812). Code for Groningen SHRA is found at https://github.com/TNO/SHRA-Groningen-seismic-so urce-model.

REFERENCES

Acosta, M., Avouac, J.-P., Smith, J.D., Sirorattanakul, K., Kaveh, H. & Bourne, S.J., 2023. Earthquake nucleation characteristics revealed by seismicity response to seasonal stress variations induced by gas production at groningen, *Geophys. Res. Lett.*, 50(19), e2023GL105455. doi:10.1029/2023GL105455

Atkinson, J., 1993. The Mechanics of Soils and Foundations, CRC press.

- Bierman, S., Kraaijeveld, F. & Bourne, S., 2015. Regularized direct inversion to compaction in the Groningen reservoir using measurements from optical leveling campaigns, NAM Report SR, 15, 11194.
- Bourne, S. & Oates, S., 2017. Extreme threshold failures within a heterogeneous elastic thin sheet and the spatial-temporal development of induced seismicity within the groningen gas field, *J. Geophys. Res. Solid Earth*, 122(12), 10–299.
- Bourne, S., Oates, S. & Van Elk, J., 2018. The exponential rise of induced seismicity with increasing stress levels in the Groningen gas field and its implications for controlling seismic risk, *J. Geophys. Int.*, 213(3), 1693– 1700
- Bourne, S.J. & Oates, S.J., 2020. Stress-dependent magnitudes of induced earthquakes in the Groningen gas field, *J. Geophys. Res. Solid Earth*, **125**(11), e2020JB020013 doi:10.1029/2020JB020013.
- Candela, T. et al., 2019. Depletion-induced seismicity at the groningen gas field: Coulomb rate-and-state models including differential compaction effect, J. Geophys. Res. Solid Earth, 124(7), 7081–7104.
- Cassiani, G., Brovelli, A. & Hueckel, T., 2017. A strain-rate-dependent modified cam-clay model for the simulation of soil/rock compaction, *Geomech. Energy Environ.*, 11, 42–51.
- Cavalié, O., Cappa, F. & Pinel-Puysségur, B., 2023. Three decades of coastal subsidence in the slow-moving nice Côte d'azur airport area (France) revealed by insar (interferometric synthetic-aperture radar): insights into the deformation mechanism, *Natural Hazards and Earth System Sciences*, 23(10), 3235–3246.
- Coppersmith, K., Ake, J., Bungum, H., Dahm, T., Main, I., McGarr, A., Wong, I. & Youngs, B., 2022. Second report from the expert panel on maximum magnitude estimates for probabilistic seismic hazard and risk modelling in Groningen gas field, Tech. Rep., Nederlandse Aardolie Maatschappij.
- Davis, S.D., Nyffenegger, P.A. & Frohlich, C., 1995. The 9 april 1993 earthquake in south-central Texas: Was it induced by fluid withdrawal?, Bull. seism. Soc. Am., 85(6), 1888–1895.
- De Waal, J. & Smits, R., 1988. Prediction of reservoir compaction and surface subsidence: field application of a new model, *SPE Formation Evaluation*, **3**(02), 347–356.
- de Waal, J.A., 1986. On the rate type compaction behaviour of sandstone reservoir rock, *Ph.D. thesis*, Technische Hogeschool Delft Delft, Netherlands
- Dempsey, D. & Suckale, J., 2017. Physics-based forecasting of induced seismicity at Groningen gas field, the Netherlands, *Geophys. Res. Lett.*, 44(15), 7773–7782.
- Dieterich, J., 1994. A constitutive law for rate of earthquake production and its application to earthquake clustering, J. Geophys. Res. Solid Earth, 99(B2), 2601–2618.
- Eaton, B.A., 1969. Fracture gradient prediction and its application in oilfield operations, J. Petrol. Technol., 21(10), 1353–1360.
- Fjaer, E., Holt, R.M., Horsrud, P. & Raaen, A.M., 2008. Petroleum Related Rock Mechanics, Elsevier.
- Fokker, P.A., Van Leijen, F.J., Orlic, B., Van Der Marel, H. & Hanssen, R.F., 2018. Subsidence in the dutch wadden sea, *Netherlands J. Geosci.*, 97(3), 129–181.
- Hangx, S. & Pijnenburg, R., 2023. Compaction in the Groningen gas field: an overview of our understanding of the compaction behaviour of the Slochteren sandstone and surroundings during and after production, Tech. Rep., Nederlandse Aardolie Maatschappij.
- Haug, C., Nüchter, J.-A. & Henk, A., 2018. Assessment of geological factors potentially affecting production-induced seismicity in north German gas fields, *Geomech. Energy Environ.*, 16, 15–31.
- Heimisson, E.R., Smith, J.D., Avouac, J.-P. & Bourne, S.J., 2022. Coulomb threshold rate-and-state model for fault reactivation: application to induced seismicity at Groningen, *J. Geophys. Int.*, 228(3), 2061–2072.
- Hettema, M., Papamichos, E. & Schutjens, P., 2002. Subsidence delay: field observations and analysis, Oil Gas Sci. Technol., 57(5), 443–458.
- Hol, S., Mossop, A., Van der Linden, A., Zuiderwijk, P. & Makurat, A., 2015. Long-term compaction behaviour of permian sandstones—an investigation into the mechanisms of subsidence in the Dutch Wadden sea,

- in ARMA US Rock Mechanics/Geomechanics Symposium, pp. ARMA-2015, Arma.
- Isotton, G., Teatini, P., Ferronato, M., Janna, C., Spiezia, N., Mantica, S. & Volonte, G., 2019. Robust numerical implementation of a 3-D rate-dependent model for reservoir geomechanical simulations, *Int. J. Numer. Anal. Methods Geomech.*, 43(18), 2752–2771.
- Jiang, Z. & Wang, H., 2022. Study on shear creep characteristics and creep model of soil-rock mixture considering the influence of water content, *Front. Phys.*, 10, 819709. doi:10.3389/fphy.2022.819709
- Kaveh, H., Batlle, P., Acosta, M., Kulkarni, P., Bourne, S.J. & Avouac, J.P., 2024. Induced seismicity forecasting with uncertainty quantification: application to the Groningen gas field, *Seismol. Res. Lett.*, 95(2A), 773–790
- Kraaijpoel, D., Martins, J.E., Osinga, S., Vogelaar, B. & Breunese, J., 2022. Statistical analysis of static and dynamic predictors for seismic b-value variations in the Groningen gas field, *Netherlands J. Geosci.*, **101**, e18. doi:10.1017/njg.2022.15
- Kühn, D., Hainzl, S., Dahm, T., Richter, G. & Rodriguez, I.V., 2022. A review of source models to further the understanding of the seismicity of the groningen field, *Netherlands J. Geosci.*, 101, e11. doi:10.1017/njg.2022.7
- Landman, A.J. & Vissers, C., 2023. Groningen dynamic model update v7, Tech. Rep. EP202306200914, Nederlandse Aardolie Maatschappij.
- Mossop, A., 2012. An explanation for anomalous time dependent subsidence, in ARMA US Rock Mechanics/Geomechanics Symposium, pp. ARMA–2012. ARMA.
- Mulders, F. M.M., 2003. Modelling of stress development and fault slip in and around a producing gas reservoir, *Ph.D. thesis*, Delft University of Technology.
- Musso, G., Volonté, G., Gemelli, F., Corradi, A., Nguyen, S., Lancellotta, R., Brignoli, M. & Mantica, S., 2021. Evaluating the subsidence above gas reservoirs with an elasto-viscoplastic constitutive law. Laboratory evidences and case histories, *Geomech. Energy Environ.*, 28, 100246. doi:10.1016/j.gete.2021.100246
- NAM, 2021. Groningen long term subsidence forecast, Tech. Rep. EP202008201822, Nederlandse Aardolie Maatschappij, version 2.
- Nguyen, V., Gland, N., Dautriat, J., David, C., Wassermann, J. & Guelard, J., 2014. Compaction, permeability evolution and stress path effects in unconsolidated sand and weakly consolidated sandstone, *Int. J. Rock Mech. Mining Sci.*, 67, 226–239.
- Ogata, Y., 2011. Significant improvements of the space-time ETAS model for forecasting of accurate baseline seismicity, *Earth Planets Space*, **63**, 217–229
- Pennington, W.D., Davis, S.D., Carlson, S.M., DuPree, J. & Ewing, T.E., 1986. The evolution of seismic barriers and asperities caused by the depressuring of fault planes in oil and gas fields of south Texas, *Bull. seism. Soc. Am.*, 76(4), 939–948.
- Pijnenburg, R., Verberne, B., Hangx, S. & Spiers, C., 2019. Inelastic deformation of the Slochteren sandstone: stress–strain relations and implications for induced seismicity in the Groningen gas field, *J. Geophys. Res. Solid Earth*, 124(5), 5254–5282.
- Pruiksma, J., Breunese, J., van Thienen-Visser, K. & De Waal, J., 2015. Isotach formulation of the rate type compaction model for sandstone, *Int. J. Rock Mech. Mining Sci.*, 78, 127–132.
- Richter, G., Hainzl, S., Dahm, T. & Zöller, G., 2020. Stress-based, statistical modeling of the induced seismicity at the groningen gas field, the netherlands, *Environ. Earth Sci.*, 79(11), 252. doi:10.1007/s12665-020-08941-4
- Roest, J. & Mulders, F., 2000. Overview modelling gas production-induced seismicity mechanisms, in *Proc. Eurock 2000 Symp., Aachen Germany*, pp. 333–338, Verlag Glückauf
- Schorlemmer, D., Gerstenberger, M., Wiemer, S., Jackson, D. & Rhoades, D., 2007. Earthquake likelihood model testing, *Seismol. Res. Lett.*, **78**(1), 17–29
- Shinohara, T., 2024. Rate-dependent deformation behaviour of porous sandstones at reservoir conditions: an experimental, numerical and microphysical study, *Ph.D. thesis*, Universiteit Utrecht.
- Shinohara, T., Jefferd, M., Spiers, C.J. & Hangx, S.J., 2024. The effect of strain rate on inelastic strain development in porous sandstones deformed

under reservoir conditions, *Int. J. Rock Mech. Mining Sci.*, **184**, 105 947. doi:10.1016/j.ijrmms.2024.105947

Smith, J.D., Avouac, J.-P., White, R.S., Copley, A., Gualandi, A. & Bourne, S., 2019. Reconciling the long-term relationship between reservoir pore pressure depletion and compaction in the Groningen region, *J. Geophys. Res. Solid Earth*, 124(6), 6165–6178.

Smith, J.D., Heimisson, E.R., Bourne, S.J. & Avouac, J.-P., 2022. Stress-based forecasting of induced seismicity with instantaneous earthquake failure functions: applications to the Groningen gas reservoir, *Earth planet. Sci. Lett.*, 594, 117 697. doi:10.1016/j.epsl.2022.117697

Suckale, J., 2009. Chapter 2 - Induced seismicity in hydrocarbon fields, in Advances in Geophysics, Vol. 51, pp. 55–106, Elsevier.

TNO, 2013. Toetsing van de bodemdalingsprognoses en seismische hazard ten gevolge van gaswinning van het groningen veld, Tech. Rep. TNO 2013 R11953, TNO Netherlands Organisation for Applied Scientific Research.

TNO, 2023. Publieke seismische dreigings- en risicoanalyse groningen gasveld 2023, Tech. Rep. TNO 2023 R10682, TNO Netherlands Organisation for Applied Scientific Research.

van Eijs, R.M. & van der Wal, O., 2017. Field-wide reservoir compressibility estimation through inversion of subsidence data above the Groningen gas field, *Netherlands J. Geosci.*, **96**(5), s117–s129.

van Thienen-Visser, K. & Breunese, J., 2015. Induced seismicity of the Groningen gas field: history and recent developments, *Leading Edge*, 34(6), 664–671.

van Thienen-Visser, K. & Fokker, P.A., 2017. The future of subsidence modelling: compaction and subsidence due to gas depletion of the Groningen gas field in the Netherlands, *Netherlands J. Geosci.*, **96**(5), s105–s116.

van Thienen-Visser, K., Pruiksma, J. & Breunese, J., 2015. Compaction and subsidence of the Groningen gas field in the Netherlands, *Proc. Int. Assoc. Hydrol. Sci.*, 372(372), 367–373.

Van Wees, J., Buijze, L., Van Thienen-Visser, K., Nepveu, M., Wassing, B., Orlic, B. & Fokker, P., 2014. Geomechanics response and induced seismicity during gas field depletion in the Netherlands, *Geothermics*, 52, 206–219.

Vermeer, P. & Neher, H., 1999. A soft soil model that accounts for creep, Beyond 2000 in Computational Geotechnics, pp. 249–261, ed. Brinkgreve, RBJ., Balkema, Rotterdam.

Wood, D.M., 1990. Soil Behaviour and Critical State Soil Mechanics, Cambridge University Press.

Zenodo, 2023. Data for TNO modelchain for Groningen.

Zoback, M.D., 2010. Reservoir Geomechanics, Cambridge University Press.

APPENDIX A: RESERVOIR DEPTH MAP

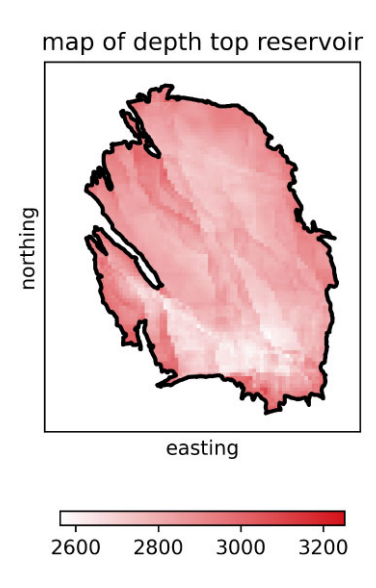


Figure A1. Depth of the top of the Groningen reservoir.

APPENDIX B: ANALYTICAL SOLUTION: ELASTIC-VISCOPLASTIC MODEL IS EQUAL TO ELASTIC MODEL

Here, we aim to find for which pair of parameters $\sigma_{h,0}^{\text{eff}}$ and M the horizontal stress history of the elastic-viscoplastic thin sheet model is equal to that of the elastic thin sheet model. The horizontal stress in the elastic-viscoplastic thin sheet model reverts to the horizontal stress of the elastic thin sheet model (eq. 7) when the second term in eqs (22) or (25) is zero:

$$\dot{\varepsilon}_{1D}^{i} \left(\frac{\frac{1}{2} \frac{\partial P^{*}}{\partial Q} + \frac{1}{3} \frac{\partial P^{*}}{\partial P}}{\frac{\partial P}{\partial Q} - \frac{1}{3} \frac{\partial P^{*}}{\partial P}} \right) = 0. \tag{B1}$$

We treat the inelastic strain rate as a given observable, so $\dot{\varepsilon}_{1D}^i \neq 0$. Thus, the numerator in the fraction term has to equal zero to retrieve the elastic solution. We use the Cam-clay formulation (eq. 29) for the partial derivatives $\frac{\partial P^*}{\partial P}$ and $\frac{\partial P^*}{\partial Q}$. With this, we can write the numerator explicitly in terms of the effective principal stresses (using eq. 5) so that $\sigma_{h,0}^{\rm eff}$ can appear later, and equal it to zero:

$$\frac{3(\sigma_{v}^{\text{eff}} - \sigma_{h}^{\text{eff}})}{M^{2}(2\sigma_{h}^{\text{eff}} + \sigma_{v}^{\text{eff}})} + \frac{1}{3} \left(1 - \frac{1}{M^{2}} \left(\frac{3(\sigma_{v}^{\text{eff}} - \sigma_{h}^{\text{eff}})}{2\sigma_{h}^{\text{eff}} + \sigma_{v}^{\text{eff}}} \right)^{2} \right) = 0.$$
(B2)

With some algebra, it follows that

$$M^{\text{elastic}} = 3\sqrt{\left(\frac{\sigma_{\text{v}}^{\text{eff}} - \sigma_{\text{h}}^{\text{eff}}}{2\sigma_{\text{h}}^{\text{eff}} + \sigma_{\text{v}}^{\text{eff}}}\right)^2 + \frac{\sigma_{\text{v}}^{\text{eff}} - \sigma_{\text{h}}^{\text{eff}}}{2\sigma_{\text{h}}^{\text{eff}} + \sigma_{\text{v}}^{\text{eff}}}}.$$
(B3)

Here, M^{elastic} is the specific value where it reproduces the elastic solution. The general expression of the effective principal stresses is

$$\sigma^{\text{eff}} = \sigma^{\text{eff},0} + \int \sigma^{\text{eff}} dt, \tag{B4}$$

where the integral for the vertical effective stress is known from the pressure history, and the integral for the horizontal effective stress is obtained by solving ODE (22) or (25). For the specific case where σ_h^{eff} is equal to the elastic solution, it is linearly proportional to the vertical stress change (eq. 7), that is,

$$\sigma_{\rm v}^{\rm eff} = \sigma_{\rm v}^{\rm eff,0} + \Delta \sigma_{\rm v}^{\rm eff},$$

$$\sigma_{\rm h}^{\rm eff} = \sigma_{\rm h}^{\rm eff,0} + \Delta \sigma_{\rm h}^{\rm eff} = \sigma_{\rm h}^{\rm eff,0} + \frac{\nu}{1-\nu} \Delta \sigma_{\rm v}^{\rm eff}.$$
(B5)

The ratio of the initial effective principal stresses, also known as the pre-consolidation ratio in geotechnical engineering, is

$$k_0 = \frac{\sigma_{\rm h}^{\rm eff,0}}{\sigma_{\rm v}^{\rm eff,0}}.\tag{B6}$$

Combining eqs (B3), (B5) and (B6) gives us

$$M^{\text{elastic}} = 3 \sqrt{\left(\frac{\sigma_{\text{v,0}}^{\text{eff}}(1-k_0) + \Delta\sigma_{\text{v}}^{\text{eff}}\left(1-\frac{\nu}{1-\nu}\right)}{\sigma_{\text{v,0}}^{\text{eff}}(1+2k_0) + \Delta\sigma_{\text{v}}^{\text{eff}}\left(1+2\frac{\nu}{1-\nu}\right)}\right)^2 + \frac{\sigma_{\text{v,0}}^{\text{eff}}(1-k_0) + \Delta\sigma_{\text{v}}^{\text{eff}}\left(1-\frac{\nu}{1-\nu}\right)}{\sigma_{\text{v,0}}^{\text{eff}}(1+2k_0) + \Delta\sigma_{\text{v}}^{\text{eff}}\left(1+2\frac{\nu}{1-\nu}\right)}}.$$
(B7)

APPENDIX C: MODEL CALIBRATION: POSTERIOR DISTRIBUTIONS

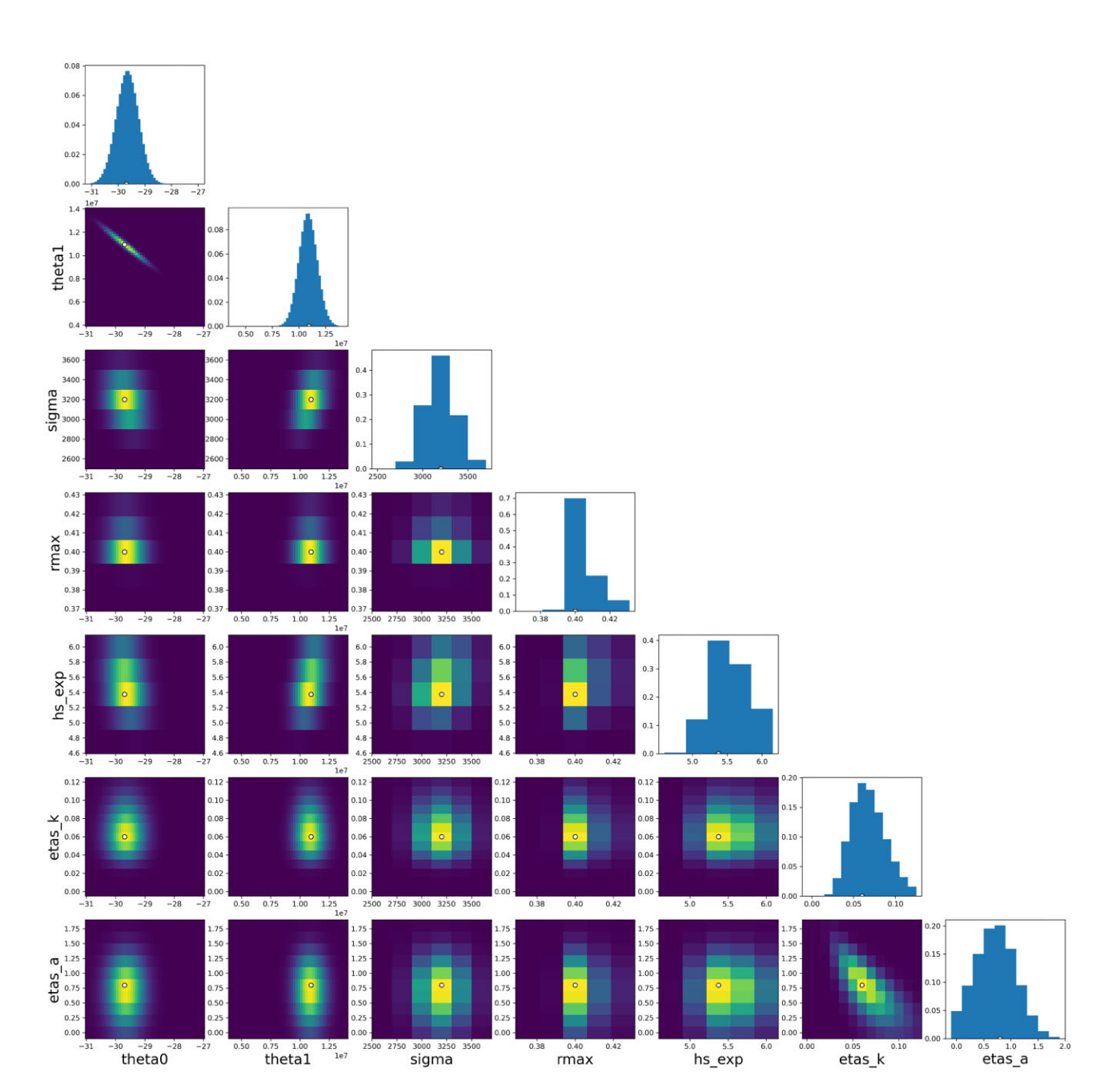


Figure C1. Marginalized posterior distributions for the linear elastic stress model, activity rate model, and ETAS parameters.

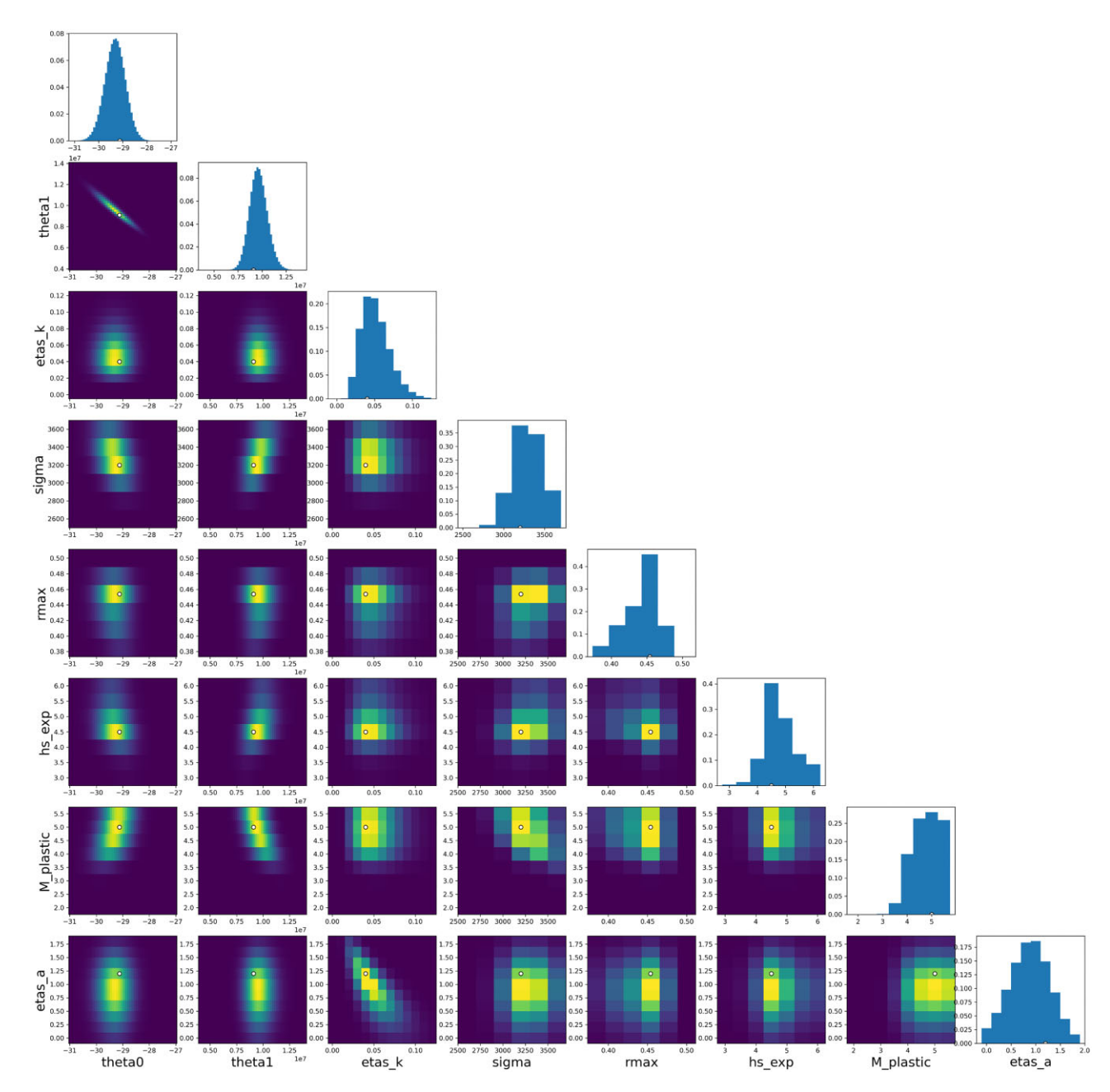


Figure C2. Marginalized posterior distributions for the elastic-viscoplastic stress model, activity rate model and ETAS parameters.

APPENDIX D: COULOMB STRESS THRESHOLD RATE-AND-STATE ACTIVITY RATE MODEL

To illustrate the difference between employing a temporal likelihood function and a spatio-temporal likelihood function in the context of calibrating the Heimisson *et al.* (2022) formulation of the rate-and-state model (which includes a threshold stress below which the seismicity rate is zero), let us consider the modelled stress values at the space-time location of the observed events. The exact values will of course depend on the stress model being used, but the principle applies broadly for any stress model. In (Fig. 2a in Bourne & Oates 2020), we see the Coulomb stress values at each observed event. Note that, regardless of the particularities of the stress model, there is always an observed event which is concurrent with the lowest Coulomb stress value (in the case of Bourne & Oates 2020), this is a value ΔS_{low} close to 0.03 MPa, while the majority of the events get assigned a Coulomb stress value between 0.6 and 1.0 MPa.

The log-likelihood function (eq. 40) requires the modelled rate at each observed event. If the log-likelihood function is defined as being temporal, this modelled rate (by definition) refers to the temporal rate, in other words, a sum over all model dimensions (such as space and magnitude) except time; the modelled rate at the time of the observed event. If the log-likelihood function is defined to be spatio-temporal, the modelled rate refers to the spatio-temporal rate; the modelled rate at the time and location of the observed event.

Since the threshold stress parameter ΔS_c is a global scalar parameter, this means that when using a spatio-temporal log-likelihood function, threshold stress values $\Delta S_c \geq \Delta S_{low}$ lead to zero likelihood (ll = -inf), since the modelled rate at the space-time location of the event is

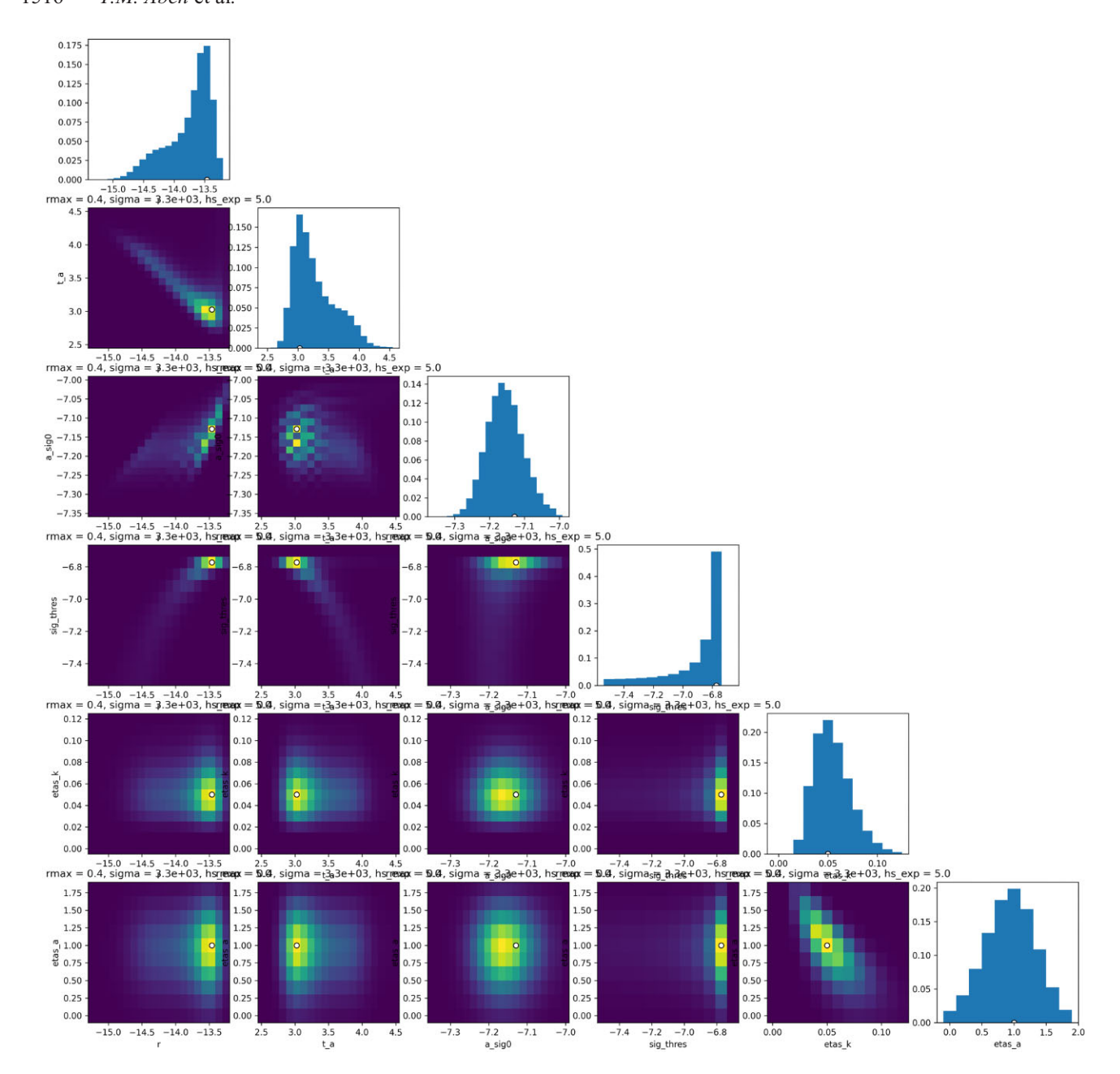


Figure D1. Marginalized posterior distributions for the elastic stress model by Bourne & Oates (2017), the activity rate model Coulomb stress threshold rate-and-state activity rate model by Heimisson et al. (2022), and ETAS parameters.

zero. However, when using a temporal likelihood function, threshold stress values $\Delta S_c \geq \Delta S_{low}$ are allowed, since it is the total field-wide rate which gets used in the likelihood function. Since both the spatial and the temporal signature of seismicity are of importance to seismic hazard and risk analysis, we believe it is unjustified to use a temporal likelihood function to calibrate the threshold rate-and-state model (or any other model for that matter). In the case of the threshold rate-and state-model, this leads to assigning non-zero (and even high) probability to models (i.e. model parameters) which forecast zero seismicity at space-time locations of observed events, whereas these models should be assigned zero probability, based on their likelihood.

When applying the spatio-temporal likelihood function to the threshold rate and state model, combined with the thin sheet stress model, we obtain a probability distribution for ΔS_c which centres around very low values and goes to zero probability at ΔS_{low} (Fig. D1). This leads to a posterior predictive seismicity model which very much resembles a classical Dieterich rate and state model (Fig. D2), with all the associated issues when applied to Groningen (e.g. Candela *et al.* 2019).

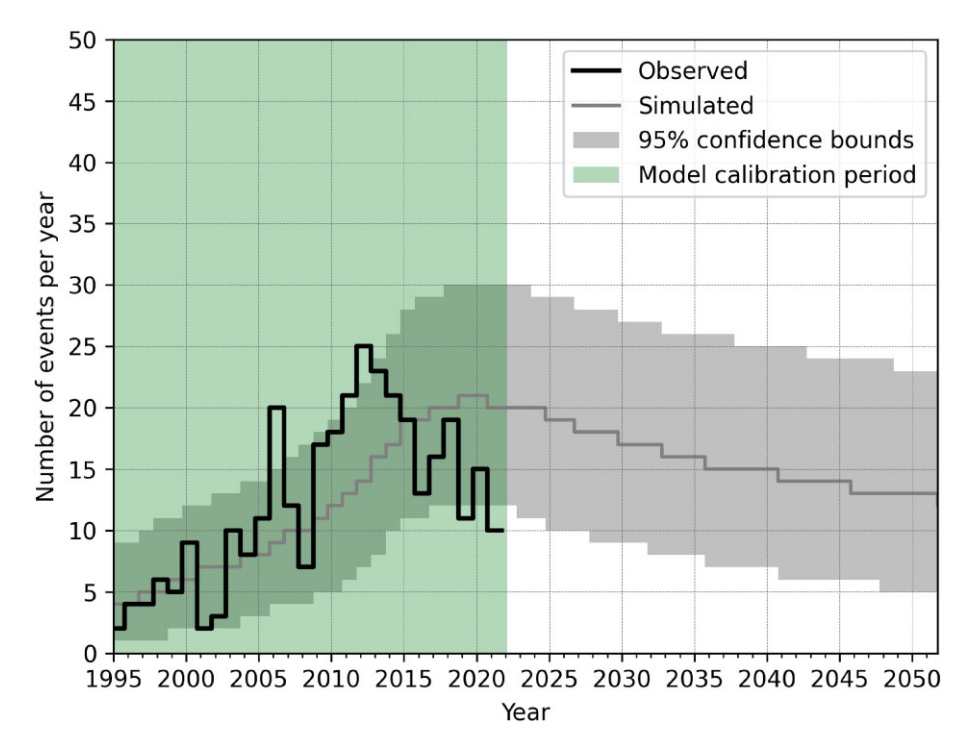


Figure D2. Modelled (grey curve) and observed (black curve) field-wide event counts for the combination of the elastic thin sheet stress model by Bourne & Oates (2017) and the Coulomb stress threshold rate-and-state activity rate model by Heimisson *et al.* (2022), with 95 per cent confidence bounds. The green coloured interval indicates the calibration period.